Three-dimensional characterisation of sedimentary heterogeneity and its impact on subsurface flow behaviour through the braided-to-meandering fluvial deposits of the Castissent Formation (late Ypresian, Tremp-Graus Basin, Spain)

Josep M. Puig[a,*], Patricia Cabello[b], John Howell[c], Pau Arbués[b]

[a]*Independent Researcher, Barcelona, Spain*

[b]*Departament de Dinàmica de la Terra i de l'Oceà, Geomodels Research Institute, Facultat de Ciències de la Terra, Universitat de Barcelona, c/Martí i Franquès s/n, 08028, Barcelona, Spain*

[c]*Department of Geology and Petroleum Geology, University of Aberdeen, Meston Building, Old Aberdeen, AB24 3UE UK*

* Corresponding author.

E-mail addresses: josepuig20@gmail.com (J.M. Puig), pcabello@ub.edu (P. Cabello), john.howell@abdn.ac.uk (J. Howell), pau.arbues@ub.edu (P. Arbués).

ABSTRACT

Fluvial deposits of the Castissent Formation (late Ypresian) form part of the Eocene infill of the Tremp-Graus piggyback basin. The Castissent Formation has been subdivided into three complexes (A, B, and C). This project focuses on the proximal fluvial-sandstones of Complex A in the Mas de Faro outcrop (NE Iberian Peninsula). There, three amalgamated channel belts are exposed in a 15 to 24 m thick succession that passes upwards from sandy braided-river deposits (A1-A2) to coarse-grained meandering-river deposits (A3). Sedimentary heterogeneities within these deposits are characterised and their impact on oil recovery in a reservoir analogue are estimated using field descriptions, virtual outcrop interpretation, a 3D geocellular facies model and fluid-flow simulations. Petrophysical values of different facies types were derived from well data through analogous fluvial deposits of the Eiriksson Formation, in the Norwegian North Sea. Facies analysis show a waning succession of gravel channel lags, unit-bar and dune deposits in A1; a basal mud-clast channel lag, unit-bars and dune deposits in A2, and a coarse-grained point-bar succession in A3. Flow simulation shows: a) fingering of the waterfront related to the gravel channel lag and unit-bars of A1 and A2, and the gravel bars, scour-and-fill deposits and dunes of A3, which act as thief zones hindering efficient sweeping of the intervals immediately above; b) segregation of the injected fluids towards the base of the channel belts due to the fining-upwards successions; and c) vertical

compartmentalization due to a relatively impermeable barrier at mud-clast channel lag beds. Permeability contrasts trapped 35% of the original oil in place after 0.5-0.6 pore volumes were injected.

Keywords: Sandy braided river, coarse-grained point bar, sedimentary heterogeneity, 3D geocellular models, flow simulation, thief zones, compartmentalization, original oil in place

1. Introduction

Fluvial deposits form important hydrocarbon reservoirs (Bridge, 2001), which commonly exhibit a high degree of heterogeneity (Tyler and Finley, 1991) at a variety of scales (Keogh *et al.,* 2014). The key heterogeneity is the porosity and permeability contrast between channel and overbank deposits. Channel bodies are generally reservoir and the overbanks tend to be non-reservoir. Significant heterogeneity can also occur within the channel deposits. This is less well understood as it typically occurs below the resolution of reservoir modelling cells and is more difficult to quantify. Multi-scale reservoir modelling (Nordhal and Ringrose, 2008; Ringrose and Bentley, 2015) provides a methodology to more accurately capture the impact of small scale heterogeneities and to bridge the gap between cm scale core plug measurements and cells in a traditional geomodel (10s to 100s of meters). Multi-scale modelling requires a detailed understanding of the intra-sandbody facies geometries.

Outcrops have long been used as analogues for subsurface deposits and they are commonly used to characterise facies architecture (see Howell *et al.,* 2014 for review). Depositional facies are the main control on reservoir performance because they control the distribution of porosity, the architecture of the permeability pathways and the presence of internal impermeable barriers (Miall, 1988). The nature of the parent channel at the time of deposition controls the distribution of facies within the sand-bodies, and therefore influences the permeability structure of the reservoir bodies. The current study focuses on facies and permeability architecture within sand-dominated braided rivers and coarse-grained meandering rivers.

1.1 Aims

This study focuses on the 3D characterisation of the well exposed fluvial succession of the lower Castissent Formation (late Ypresian) in the Mas de Faro outcrop, in the Tremp-Graus Basin which is part of the South Pyrenean Foreland Basin (Fig. 1). The succession is interpreted to be deposited by sand-dominated braided rivers and coarse-grained meandering rivers (see Models 5 and 10 in Miall, 1985 for review). The Mas de Faro outcrop lies within the proximal part of the Castissent fluvial systems and is characterised by a 15 – 24 m thick amalgamated

fluvial channel-belt succession. Detailed analysis illustrates that the channel deposits contain laterally continuous clast-supported gravels and mud-clast conglomerate intervals which define high permeability thief zones and barriers, respectively.

The high quality of the exposure and its lateral extent offers a good opportunity to study the geometry and potential impact of these heterogeneities on fluid-flow at the intra-channel scale.

The aims of this paper are to document the sedimentary heterogeneities in the studied succession by building on previous studies by Nijman and Nio (1975), Nijman and Puigdefàbregas (1978) and Marzo *et al.,* (1988), and to estimate their influence on reservoir production by using geocellular modelling and fluid-flow simulations. These objectives were achieved by combining traditional field descriptions with drone-derived, photogrammetric virtual outcrops. These data were used to map the distribution of the sedimentary bodies in three dimensions. Petrophysical properties, from the analogous Eiriksson Formation in the North Sea were added to the outcrop models for reservoir flow simulation.

2. Geological setting

2.1 The Southern Pyrenees and the Tremp-Graus Basin

The Pyrenees is an east–west orogenic belt developed due to collision of the Iberian and the European plates during the Late Cretaceous–middle Miocene Alpine orogeny. This collision inverted the previous Mesozoic extensional rift basins (Vergés and Muñoz, 1990; Muñoz, 1992; Muñoz, 2002; Saura *et al.,* 2016). The Pyrenees can be divided into three main zones: the Northern Pyrenees, characterised by northward propagating thrusts; the antiformal stack of the Axial Zone in the centre; and the Southern Pyrenees, a southwards-verging thrust-and-fold belt (Séguret, 1972; Vergés and Muñoz, 1990). From north to south, the Southern Pyrenees are made up of the Bóixols thrust sheet, which was emplaced during the Late Cretaceous, the Montsec thrust sheet, which developed during the Palaeocene–early Eocene, and the Serres Marginals thrust sheet, which was emplaced in the middle Eocene to the Oligocene (Cámara and Klimowitch, 1985; Muñoz, 1992; Muñoz, 2002) (Fig. 1). The foreland basin in front of the Southern Pyrenees is subdivided by lateral anticlines into three sub-basins. The Tremp–Graus Basin is the most easterly of these and was structured as a piggyback basin on top of the Montsec thrust sheet during the early Eocene (Puigdefàbregas *et al.,* 1992; Muñoz *et al.,* 1994). The basin forms an east-southeast–west-northwest asymmetrical syncline (Marzo *et al*., 1988; Nijman, 1998).

The sedimentary fill reaches a thickness of 2,500 m and was deposited between the Palaeocene and the upper Eocene. It is mainly comprised of alluvial, fluvial, and deltaic deposits (Nijman, 1998). The sedimentary evolution of the basin records an overall progradation towards the west and the fill of the basin is time equivalent to deep water deposits in the Ainsa and Jaca basins to west.

2.2 The Montanyana Group and the Castissent Formation

The Montanyana Group (Nijman and Nio, 1975) is a fluvio-deltaic system deposited in the Tremp-Graus Basin in the Ypresian to late Lutetian (Fig. 2). This fluvio-deltaic system entered the basin from the southeast and flowed towards the northwest, interfingering with alluvial fans in the northern margin (Nijman and Nio, 1975; Nijman and Puigdefàbregas, 1978; Marzo *et al*., 1988).

The Montanyana Group is subdivided into the upper, the middle and the lower Montanyana Sub-Groups (Fig. 2). The lower and the upper Montanyana Sub-Groups are composed of alluvial plain and upper delta plain deposits that grade laterally to lower delta plain and delta front deposits towards the west-northwest. The middle Montanyana Sub-Group is composed of the fluvial deposits of the Castissent Formation that record a marked progradation of the clastic wedge, forced by hinterland tectonics during a highstand period (Nijman, 1998). The Castissent Formation (Van Eden, 1970) is up to 150 m thick and is upper Ypresian in age. It is traditionally subdivided into three different multi-lateral and multi-storey sheet sandstone complexes, named A, B, and C, which are encased in fine-grained deposits (Nijman and Puigdefàbregas, 1978; Marzo *et al*., 1988; Nijman, 1998). These sandstone complexes are separated by four brackish marls that record marine onlaps. Each complex is approximately 25 – 30 m thick and 4 – 6 km wide.

In the proximal portion of the basin, the sandstone complexes A and B are closely stacked, attaining a combined thickness of 50 to 90 m, whereas Unit C is absent.

2.3 The Mas de Faro Outcrop

The Mas de Faro outcrop is located in Catalonia, in the region of the Pallars Jussà, in the province of Lleida, close to the border with Aragon (Fig. 3). It is situated 5 km to the east of the Pont de Montanyana village, on the C-1311 road.

At basin scale, the Complex A is composed of three different channel belts, A1, A2 and A3, separated by floodplain deposits (see Fig.12 in Marzo *et al*., 1988). In the Mas de Faro outcrop, located in the proximal portion of the fluvial system, these appear as amalgamated sheet bodies. Nijman and Nio (1975) suggested that the Castissent

Complex A resulted from a single river channel, showing a characteristic coarse-grained point-bar structure like the modern Amite and Colorado Rivers in Texas (McGowen and Garner, 1970) and in the River Endrick in Scotland (Bluck, 1971). The channel deposits of A1 and A2 were subsequently re-interpreted as the deposits of a bedload-dominated braided river with A3 dominated by low sinuosity, coarse-grained point-bar deposits (Nijman and Puigdefàbregas, 1978; Marzo *et al.*, 1988).

3. Methods

3.1 Outcrop study

The dataset for this study comprises 9 stratigraphic logs collected at a scale of 1:50 (MD1 to MD9; Fig. 3), palaeocurrent measurements from 500 locations and a virtual outcrop model. The outcrop model, generated using structure-from-motion photogrammetry from images acquired using an Unnamed Aerial Vehicle (UAV), covers 900 m of nearly continuous outcrop (Chesley *et al.,* 2017).

Agisoft PhotoScan (by Agisoft LLC) was used to process the acquired images, reconstruct the geometry of the outcrop and create a 3D textured mesh. The photogrammetry model was edited in Polyworks (by Innovmetric) to fill small gaps within the mesh, and imported into LIME, a 3D interpretation software (Buckley *et al.,* 2018) used to digitize the stratigraphic log traces with facies interpretation, position of the palaeocurrent measurements and map the key stratigraphic surfaces.

Eleven sedimentary facies were identified from the logs and mapped on the virtual outcrop. This mapping subdivided the succession into stratigraphic intervals that record distinct sedimentary processes and fluvial environments.

The outcrop model and the digitized data were imported into MOVE (by Petroleum Experts Ltd.) and were backtilted in order to remove the tectonic dip (2.83° dipping towards N278.76°).

3.2 Petrophysical data

The petrophysical data used in this study were taken from publicly available core descriptions and analysis of the Eiriksson Formation of the Statfjord group in the Norwegian North Sea (Norwegian Petroleum Directorate, 2016). Porosity, permeability and fluid saturation values were compiled and related by regression to the Castissent grain-size and facies logs (see Section 5.2).

3.3 3D geocellular models and fluid-flow simulations

The outcrop model and associated facies, porosity and permeability logs were imported into the Petrel modelling software (by Schlumberger). Bed contacts mapped using Lime and structurally restored in Move were used to construct stratigraphic horizons in three-dimensions. These horizons provided a framework for the 3D grid construction and subdivision in zones. 3D geocellular facies and petrophysical models were built based on the log data. Petrophysical models were used to perform fluid-flow simulations.

4. Stratigraphy and sedimentology of Castissent Complex A in the Mas de Faro outcrop

4.1 Facies

A facies is defined as a body of rock with similar grain size, composition, geometry and scale of sedimentary structures (Collinson, 1969). Eleven facies are defined in this study based on lithology, sedimentary structures, grain size and facies thickness. Facies properties are summarized in Table 1 and Fig. 4. These include three conglomerate facies (**Mcgl, Gm, and Gt/Gp**), six sandstone facies (**Sp1, Sp2, St1, St2, Sr,** and **Sh**) and one mudstone facies (**Fm**).

4.2. Fluvial architecture and hierarchy of bedding scales.

The hierarchy scheme used in this study is slightly modified from previous classifications of Campbell (1967), Friend *et al.,* (1979), Marzo *et al.,* (1989) and Ford and Pyles (2014). A short summary and definition of the different scales is presented, for further details the reader is referred to the studies mentioned above. A *lamina* is a relatively uniform layer in composition and texture, which is not internally layered and that generates in a much shorter time than the enclosing bed (Campbell, 1967). *Lamina-sets* are conformable sets of lamina, thinner than a bed, separated by conformable, erosive or non-deposition surfaces and that generate distinctive structures within a bed (Campbell, 1967). *Beds* are layers containing genetically related lamina-sets, which are bounded by bedding surfaces, which represent periods of non-deposition or abrupt changes in depositional conditions (Campbell, 1967). *Bed-sets* are composed of two or more superposed beds showing similar composition, texture and sedimentary structures (Campbell, 1967). *Stories* are composed of genetically related beds or bed-sets formed by the migration or fill of a fluvial channel with thicknesses comparable to the bankfull water depth and characterised by erosional lower bounding surfaces (Table 2) (Friend *et al.,* 1979; Ford and Pyles, 2014). C*hannel belts* are composed of one or more vertically or laterally stacked stories produced by channel migration or fill. They are the result of long-term

landscape evolution, and are defined by river avulsions (modified from Ford and Pyles, 2014). Finally, *complexes* are composed of two or more amalgamated channel belts (Marzo *et al.*, 1988).

4.3 Description of the sedimentary architecture and channel-belt deposits

The Complex A is vertically bounded by thick mudstone deposits. It is composed of three amalgamated channel belts with a sheet like geometry A1, A2, and A3, separated by erosional surfaces. (Fig. 5).

A typical section compiling the observations and interpretations of the Castissent fluvial succession at the Mas de Faro outcrop is presented in Fig. 6.

4.3.1 A1 Channel belt

Channel belt A1, 5 to 9 m thick, exposes a single-story containing two fining-upwards alternations of facies Sp1 and St1. The first (Fig. 5 and Fig. 6) has a 0.6 to 2.6 m thick, massive to poorly-bedded, basal deposit (facies **Gm;** Table 1) consisting of clast-supported, sub-rounded to rounded pebbles and cobbles with sand matrix and minor amounts of mud-clasts and oxidized wood fragments. Small gutters are observed along the basal erosion surface cut into the underlying mudstone (facies **Fm**). The basal gravels are overlain by a 1.5 to 3.5 m thick, pebbly-to-coarse sandstone with 1 to 4 large-scale planar-asymptotic cross-stratified beds (facies **Sp1**). Beds are 0.4 and 3 m thick. Internally, beds are composed of lamina-sets, which are a few cm thick and show fining-upwards patterns. Grain size along lamina is coarser in their lower side than in the upper side. Subordinate amounts of mud-clasts and oxidized organic fragments up to 1 m length were observed.

A 2 m thick bed-set, pebbly-to-medium sandstone dominated (facies **St1**), with 0.2 to 0.6 m thick trough cross-laminated beds is located on top. Medium grained sandstone deposits are better preserved than pebbly-to-coarse sandstones. The second alternation (Fig. 5 and Fig. 6) is finer-grained overall than the first. The basal deposits generally are cross-laminated coarse sandstones with subordinate pebbles (facies **Sp1**). The large-scale planar-asymptotic cross-laminated beds are 0.5 and 1.5 m thick. These deposits are capped by small-scale trough cross-laminated coarse-to-medium sandstone beds, which contain thin laminae of oxidized organic matter (facies **St1**).

4.3.2 A2 Channel belt

Channel belt A2, 1 to 4.5 m thick, exposes a single-story (Fig. 5 and Fig. 6). An overall fining-upwards trend is observed within the exposed channel-belt deposits. A distinctive massive mud-clast and pebble basal facies (**Mcgl**)

is 0.2 to 1.5 m thick. The 1 to 10 cm diameter, sub-angular to sub-rounded, mud-clasts are black. Mudstone blocks up to 0.5 m large rarely occur.

Pebbly-to-coarse sandstones in the middle part of A2 (facies **Sp1**) contain 1 to 3, 0.5 to 2 m thick, large-scale planar-asymptotic cross-stratified beds. The capping facies are poorly exposed trough cross-stratified, pebbly-to-medium sandstones (facies **St1**).

4.3.3 A3 Channel belt

Channel belt A3, 5 to 9.5 m thick, exposes a single-story. It can be subdivided into: a basal interval with gravel facies (facies **Gp** and **Gt**) and minor amounts of trough cross-laminated sandstones (facies **St1**), a middle interval with planar cross-laminated upper coarse to upper medium sandstones (facies **Sp2**) and an upper finer-grained sandstone interval (Fig. 5 and Fig. 6). The top 1 and 3.5 m of this channel belt is a highly mottled sandstone with internal bedding wedges separated by accretion surfaces. This interval fines-upwards from trough cross-laminated coarse-to-medium sandstone beds (facies **St2**) to nearly horizontally-laminated medium-to-fine sandstones (facies **Sh**) and rippled cross-laminated fine sandstones on top (facies **Sr**).

4.4 Palaeocurrent analysis

There is a progressive change in mean transport direction from the northwest to the west up-section. The measured palaeocurrents (Fig. 6; Fig. 7) indicate large cross-stratified beds parallel gutter casts in A1 channel belt, showing mean palaeocurrent directions towards 311° and 313°, respectively. Large cross-stratified beds record more consistent palaeocurrent directions throughout the channel belts than small cross-stratified beds, which are characterised by a higher variability and tri-modal patterns. Measurements of accretion surfaces in A3 show a mean dip of 10° and a mean dip-azimuth of 339°, which represents a deviation of 48° and 86° compared to the mean 291° and 252° palaeocurrent directions measured in the basal and middle part of the channel belt, respectively.

4.5 Interpretation of the sedimentary architecture and channel-belt deposits

Proximal A1 channel-belt deposits were interpreted as braided-river deposits by Marzo *et al.,* (1988) after describing and correlating them along the basin. Underlying facies **Fm** is interpreted as floodplain deposits. Elongate scours filled with clast-supported gravels (facies **Gm**) are interpreted to be fluvial channel lag deposits. The almost consistent palaeocurrent orientation of these lag scours between the, widely-spaced measured sections, indicates these are deposits of a low-sinuosity river sourced from the southeast. Facies **Sp1** is interpreted as unit-bar deposits above the channel lag. Lee dips of the facies parallel the underlying lag scours, suggesting that they occurred in

the same channel and indicating downstream migration. Facies **St1** is interpreted as the resulting deposit of dunes. Dunes are interpreted to be formed coevally to unit-bar deposits. Once dunes overtake the bar crest, its charge is deposited down the lee face and form the larger scale cross-lamina and lamina-sets (Reesink and Bridge, 2007; 2011). The fact that finer-grained dune deposits in A1 are better preserved than the coarser ones implies that is not easy to recognize the genetic relationship between dunes and unit-bars, as superimposed bedforms should match the grain-size distribution observed in the large cross-stratified unit-bar deposits. However, we found locally preserved pebbly sandstone dune deposits, which match the grain size observed within unit-bar lamina-sets, directly superimposed on top. Fining upward trends along dune bed-sets are interpreted as the result of flow unsteadiness. The lack of evidences for subaerial exposure indicates that both type of deposits were formed when water was capable of overflowing the unit-bars top. Vertical alternations of unit-bars and dunes are found building up compound-bars and within single channel fills in sandy braided rivers. As pointed out by Ashworth *et al.,* (2011) there are no significant differences between them, hence it is not possible to discern between types. As a result, alternating unit-bar and dune deposits in A1 could be interpreted as compound-bar or channel-fill deposits (i.e., a downstream-accreting or channel-fill story).

After basin-scale mapping of A2 deposits by Marzo *et al.,* (1988), these were interpreted as braided-river deposits of a new channel belt. The mean 272° palaeocurrent direction indicates that it was mainly sourced from the east. The mud-clast dominated deposit (facies **Mcgl**) at the base of A2 is interpreted as a channel lag deposit, given its composition texture of the clasts, and the erosional basal surface. We suggest that the mud could have been sourced from a nearby, poorly drained, non-preserved floodplain deposit. The poorly drained conditions of the floodplain are inferred based on the dark colour of the mud-clasts. Like A1, A2 **Sp1** and **St1** facies succession is interpreted as an alternation of unit-bar and dune deposits forming part of a compound bar or channel fill.

Deposits in A3 were interpreted as coarse-grained point-bar deposits formed in a new channel belt (Nijman and Puigdefàbregas, 1978; Marzo *et al.,* 1988). The basal gravels (facies **Gt** and **Gp)** are interpreted as scour and fill deposits, and gravel bars deposited in the deepest part of the channel. The interbedded and overlying facies **St1**, is interpreted as dune deposits. The transition from gravel to sandy dune cross-stratified facies is interpreted to result from the progressive decrease in the flow energy. The mean 290° palaeocurrent direction for the basal part of the succession suggests that this renewed fluvial course was mainly sourced from the east. These facies described above correspond to the scour-and-pool conglomerates and lower-point-bar conglomeratic sandstones of Nijman and Puigdefàbregas (1978).

Facies **Sp2** found in the middle part of the succession resembles the unit-bar deposits interpreted in channel belts A1 and A2. However, we observe that in some localities this facies is laterally bounded and separated by accretion surfaces. These surfaces show a mean deviation of 87° with respect to the mean palaeocurrent value of 252° in facies **Sp2**. As a result, these are interpreted as lateral-accretion surfaces based on the spatial relationship observed (see Fig. 7). Hence, facies **Sp2** is interpreted as unit-bar deposits that formed as part of a point bar (i.e., a lateral-accreting story). These deposits correspond to the transverse bars of Nijman and Puigdefàbregas (1978). In this paper the term transverse bars is merely used in order to differentiate them from the unit-bars of A1 and A2.

The structure of the point bar and the accretion surfaces is more developed in the mottled interval found at the upper part of A3. Facies **St2**, **Sh**, and **Sr** are interpreted as dune deposits (festoons of Nijman and Puigdefàbregas, 1978), plane beds and ripples developed because of the progressive energy decrease of the helicoidal flow towards the upper parts of the point bar. These deposits correspond to the upper-point-bar festoon beds and to the inner accretionary bank of Nijman and Puigdefàbregas (1978). Overlying facies **Fm** is interpreted as floodplain deposits.

The vertical evolution of Complex A was explained by Marzo *et al*., (1988) as the result of several aggradation-degradation cycles, controlled by tectonics. The initial stage of each cycle was characterised by aggradation in bedload dominated braided rivers, and the late stages by meandering streams. These cycles were repeated for A1, A2, and A3, with the meandering-river deposits being mainly present in A3, where they were not removed by the next cycle of degradation. Coincident with these aggradation-degradation cycles was the shift of the fluvial systems towards the west–southwest as a consequence of the displacement of the basin axis due to the active tectonic regime (Puigdefàbregas *et al*., 1992; Nijman, 1998).

5. Subsurface analogue: The Eiriksson Formation (Statfjord Group, Norwegian North Sea)

5.1 Facies and fluvial styles in the Eiriksson Formation: Comparison with Castissent Complex A

The Eiriksson Formation (Hettangian – Sinemurian, Lower Jurassic) forms part of the Statfjord Group (Rhaetian – Sinemurian), which is one of the main hydrocarbon-bearing intervals in the northern North Sea (Ryseth and Ramm 1996).

The proximal fluvial deposits of the Eiriksson Formation in the Tampen Spur area (Fig. 8A) are considered a suitable subsurface analogue for the Castissent Formation based on its facies and similarities in fluvial architecture and fluvial style variations. The different facies described below are interpreted to be fluvial deposits formed in braided

and coarse-grained meandering rivers (Ryseth and Ramm, 1996; Ryseth, 2001). Fluvial architecture is characterised by amalgamated multi-storey and multilateral sheet-like channel belts, 5 to 15 m thick, and variable amounts of floodplain deposits (Ryseth and Ramm, 1996).

Channel belts described by Ryseth and Ramm (1996) (Fig. 8B) are typically composed of multiple storeys, with internal fining-upwards trends, beginning with a massive or poorly bedded deposit of facies **Gm** or **Se** found immediately above an erosional basal surface. These deposits are interpreted as gravel and coarse sandstone channel lags, scour and fill deposits, and gravel bars (Ryseth, 2001). Above the lag deposits the succession is characterised by variable amounts of interbedded trough and planar cross-stratified pebbly-to-fine sandstones (facies **St** and **Sp**), massive coarse-to-fine-grained sandstones (facies **Sm**), and horizontally laminated coarse-to-medium sandstones (facies **Shc**). Facies **Sp** and **St** are interpreted as leeside-accreting unit-bar and dune deposits, respectively (Ryseth and Ramm, 1996; Ryseth, 2001). Massive sandstones are characteristic facies in the Eiriksson Formation and are interpreted to be the result of rapid deposition and sediment dumping during flash discharge events (Ryseth and Ramm, 1996; Ryseth, 2001). Facies **Shc** are commonly found on top of the massive sandstones and are interpreted to be upper flow regime structures. The vertical succession ends up with very fine-to-fine rippled sandstones (facies **Sr**) and horizontally laminated sandstones (facies **Shf**) (Ryseth and Ramm, 1996; Ryseth, 2001). Ryseth (2001) stated that the presence of gravel lags and the high proportion of planar cross-stratified beds capped by minor amounts of trough cross-stratified beds would be indicative of deposition in sandy braided rivers. However, the localities dominated by trough cross-stratified gravels and sandstones suggests deposition within coarse-grained meandering rivers.

Comparing the facies in the Eiriksson Formation with the ones in Complex A, we suggest that the vertical successions dominated by gravels lags (facies **Gm**) and planar cross-beds (**Sp**) with interbedded trough cross-beds (**St**) may be like the channel lag, unit-bar and dune deposits interpreted in the sandy braided A1 and A2 channel belts. The successions dominated by trough cross-stratified gravels (**Gt**) and trough cross-stratified sandstones (**St**) with marked fining-upwards trends and subordinate ripples (**Sr**), and plane beds (**Sh**) could be analogous to the coarse-grained meandering point-bar deposits interpreted in A3. Nevertheless, massive sandstone beds and upper flow regime structures in the Eiriksson Formation were not recognized in the Castissent Formation.

5.2 Petrophysical rock properties from the analogous Eiriksson Formation

Petrophysical values from the outcrop were not used due to the extensive cementation. Data used were derived from the Eiriksson Formation, in order to generate results more directly related to subsurface reservoirs. The wells used were 33/9-9 from the Statfjord field, 34/10-30 from the Gullfaks Sør field and 34/10-13 from the Gullfaks field (Fig. 8A).

Lithology and grain-size logs from conventional core descriptions of the Eiriksson Formation were converted to a numerical scale and related by regression to porosity, measured on core plugs and nuclear magnetic resonance (NMR) of core chips during special core analysis. Relationships between porosity and horizontal permeability measured in the core plugs were determined by regression. Horizontal to vertical permeability ratio was also calculated from the core plug data.

Irreducible fluid saturations and relative permeabilities were derived from special core analysis that waterflooded core plugs under reservoir conditions. Porosity was related to the irreducible water saturation using Timur's equation (Timur, 1968) and to the irreducible oil saturation. Oil effective permeability at irreducible water saturation was defined from the horizontal air permeability of the rock. Finally, water effective permeability at irreducible oil saturation was defined from the oil effective permeability at irreducible water saturation.

The regressions shown in Fig. 9 were applied to the Castissent grain-size and facies logs in order to perform petrophysical modelling and to obtain the permeability functions used during the flow simulations (see Section 7.1)

6. 3D geocellular models

6.1 Description of the 3D grid

The model is 514 m wide by 514 m long by 30 m thick. A convergent interpolation method with a grid size of 0.5 by 0.5 m was selected for the horizon modelling. Thirteen stratigraphic horizons were reconstructed (Fig. 10B), defining 12 vertical zones within the grid (Fig. 10A). The lowermost and uppermost zones correspond to the floodplain deposits below and above Complex A. The horizontal dimensions of the 3D grid cells were set to 5 m by 5 m N - S oriented planview cell faces. Varying grid layering styles were applied to different zones in order to mimic the bedding observed in the outcrop and reduce aliasing (see Fig. 10A and Fig. 5). Base conformable layering was applied to zones with facies patterns that parallelled the basal surface and were top truncated at overlying erosion surfaces. Inclined internal surfaces following the mean orientation of the cross-stratification planes were used for the zones with unit-bar deposits characterised by well-developed large planar cross-stratification planes.

Proportional grid layering was used for zones with facies trends that parallel both basal and top horizons (i.e., horizon above was not erosional)

A mean cell height of 0.5 m was set up for most of the zones, except for the lower floodplain deposits, where a cell height of 3 m was selected, and for the zones with *proportional* layering (i.e., upper floodplain deposits and the accretionary bank), where the vertical subdivision must be set up by specifying the number of vertical layers, setting 10 layers for each zone. This results in a 3D grid with approximately 6.8 million cells. Upscaling to a coarser grid was not necessary for flow simulations.

6.2 Facies and petrophysical modelling

Facies, porosity and permeability logs were loaded as deviated wells and upscaled to the 3D grid. Each of the 12 zones modelled is represented by one or more type of interpreted deposits according to the sedimentary architecture described in the outcrop (see Fig. 5 and 6). For simplification, the lateral-accretion surfaces of the point bar were not modelled for the limited localities where they were observed. The unit-bar and dune deposits of A2 were modelled as a single interval.

Porosity and permeability logs were obtained by applying the regression functions from the Eiriksson Formation analysis to the continuous grain-size logs of the Castissent Formation.

For the facies log, a discrete upscaling was used such that the facies category with the greatest proportion in each cell would be assigned. The porosity and horizontal permeability logs were upscaled using the arithmetic mean, whereas the vertical permeability was upscaled using the harmonic mean. The arithmetic and harmonic means are commonly used to approximate the horizontal and vertical flow, respectively (Benson, 2015).

Model 1 assigned constant facies and interpreted deposits in each zone (Fig.10A and Fig. 5). The facies model was populated with average porosity and permeability values calculated from the upscaled logs—separately for each modelling zone.

All zones were modelled as discrete facies except the gravel lag at the base of A1, which was modelled as an object within a sand background using the dimensions collected from the outcrop (Table 3) (Lia *et al*., 1996; Falivene *et al*., 2007).

Model 2 rock properties were assigned using the Sequential Gaussian Simulation algorithm (Deutsch and Journel, 1997). Variogram analysis was necessary. The analysis was conducted on the continuous porosity logs. First, all the horizontal and vertical directional trends were removed. Subsequently, the data were transformed to a normal

distribution. Different types of variograms (Gaussian, Spherical, or Exponential) and correlation lengths were applied to find the best fit for the data.

The sill was locked at a value of 1 and the nugget value was displaced between 0 and 0.25 depending on the case. Once the horizontal variograms were set up, the vertical variograms were calculated (Table 3).

For each zone, the orientation of the variograms was locally constrained to the palaeocurrent measurements (see Fig. 7) using the "Locally Varying Anisotropy" option in Petrel. The horizontal and vertical permeability distribution was obtained by applying the regression between porosity and permeability to the stochastically modelled 3D porosity cube.

6.3 Results of the property modelling

The property models constructed for the Castissent Formation in the Mas de Faro outcrop (Fig. 11) show that the most common deposits, excluding the floodplain deposits, are the ones associated with: the unit-bars of A1 and A2 (16.47%), the gravel bars, scour and fill deposits and dunes of A3 (15.55%), followed by the dunes of A1 (13.66%), and the accretionary bank of A3 (8.26%). The less represented are the transverse bars (5.15%), the mud-clast lag (4.29%), and the gravel lag deposits (1.81%). The mud-clast lag is assumed to produce a relatively impermeable, thin and laterally continuous barrier to flow along the outcrop, which vertically subdivides Complex A into two reservoir-like intervals: A1 below, and A2 and A3, above.

Moreover, relatively impermeable facies that correspond to mudstones of the floodplain underneath A1 and on top of A3, also occur.

The petrophysical Models 1 and 2 were constrained with the same minimum and maximum values. However, some differences are identified in the distribution and representativeness of the petrophysical data in both models (Fig. 11). In Model 1, the petrophysical contrasts are only recorded in the limits of the different modelled zones, which record constant and mean petrophysical values. Model 2 shows a wider range of values, and a higher petrophysical variability is captured within each modelled zone.

7. Fluid-flow simulations

7.1 Rock pressure, relative permeability functions and development strategy

A dead-oil model was used consisting of two phases, oil and water. The oil-water contact was below the model. Bubble point pressure was set to 80 bars and maximum reservoir pressure to 300 bars, which corresponds to the fracture pressure. These pressures were the main input used to set up the limits of the rock compaction functions, which describes the changes in porosity as the pressure changes during production. The reservoir analogue reference pressure was set to 250 bars, which corresponds to a depth of 2,543 meters, the mean depth of the Eiriksson Formation in the referenced wells.

Oil and water relative permeability functions were obtained by normalizing the effective permeabilities to the effective oil permeability at irreducible water saturations. For Model 1, a relative permeability function for each type of interpreted deposit, was used. For Model 2, we used the porosity model to define the number of relative permeability functions (for every 1% increase in porosity, we constructed a relative permeability function, Fig. 12).

The flow simulations were run in Petrel using the Eclipse 100 simulator. Four five-spot well patterns were considered consisting of 9 injectors and 4 producers that were approximately 166 m apart. The water injection rate was held at 750 Sm^3/day and producers were closed when the water cut reached 90%.

7.2 Results of the fluid-flow simulation on reservoir production

In order to evaluate the impact of the facies architecture on reservoir performance, the water cut and recovery factor were plotted against the water injected pore volume for the simulations in Models 1 and 2 (Fig. 13). These results are summarized in Fig. 14. Recovery efficiency at the end of the simulations (i.e., with a water cut of 90%) is 50.41% in Model 1 and 50.58% in Model 2. Both models estimated an inflection point in productivity at around 0.15% of the injected pore volumes. Model 2 showed an earlier water breakthrough (at about 0.05% of the injected pore volumes), whereas for Model 1, the water breakthrough occurred at 0.08% at injected pore volumes. The increase in the water cut over time is more progressive for Model 1 (i.e., the water cut curve shows a gentler slope) than for Model 2. In Model 1, 14.2% of the total oil in place is unmoveable oil and 35.38% of the moveable oil is not swept at the end of the simulation. In Model 2, 14.6% of the total oil in place is unmoveable oil and 34.79% was moveable oil trapped in the reservoir analogue.

8. Discussion: Sedimentary heterogeneity impact on fluid-flow behaviour and oil recovery

8.1 Flow behaviour: flow units and permeability barriers

The mud-clast channel lag at the base of A2 acts as a flow barrier that vertically compartmentalizes Complex A. This laterally extensive layer separates A1 from A2 and A3, causing them to act as two independent flow units. Earlier works also described the impact of the presence of mud-clasts in fluvial reservoirs. North and Taylor (1996) documented that the sand-dominated ephemeral fluvial succession of the Lower Jurassic Kayenta Formation, in Utah, was compartmentalized by the presence of mud-clast lags. Jones and Hartley (1993) suggested that conglomerate lags composed of variable amounts of mud-clasts and wood fragments in the Carboniferous Pennant sandstones would also reduce the effective permeability. Henares *et al.,* (2016) show that the occurrence of variable amounts of mud-clasts within fluvial sandstones of the Triassic Bigoudine Formation, in the Argana Basin, favours early reduction of the primary porosity during mechanical compaction given its ductile behaviour, and that the presence of continuous layers between amalgamated sandstone bodies could generate local barriers for fluid-flow and could therefore compartmentalize the succession.

In the early stages of the flow simulations, two vertically separated waterfronts were generated: a) the lower waterfront in the gravel channel lag and in the basal part of the unit-bars of A1; and b) the upper waterfront in the gravel bars, scour and fill deposits and dune interval of A3 (Fig. 14). The presence of these preferential flow conduits was caused by the heterogeneous distribution of the petrophysical properties in the reservoir analogue. The high permeability contrast of the conglomeratic and very coarse-grained facies cause these deposits to act as thief zones, catching a considerable volume of the injected water and producing fingering of the waterfront and thus bypassing the surrounding areas (Fig. 14). Similar fingering effects within braided fluvial heterogeneous reservoirs have been demonstrated in flow simulations carried out in a sandy braided river exposure of the Maroon Formation in Colorado by using borehole data from the Statfjord Group in the North Sea (Høimyr *et al*., 1993). Highly permeable zones in this outcrop analogue model favour an early water breakthrough and waterfront fingering that result in a decrease of the recovery efficiency. Lunt *et al.,* (2004) stated that open-framework conglomerates (OFC) commonly form thief zones during water flooding. The porosity measurements of OFC in the gravelly-braided Sagavanirktok River, Alaska, show that they have intermediate porosities ranging from 15–25%, having very high permeabilities (1,000s to 10,000s Darcys). The heterogeneous distribution of petrophysical properties and the role of OFC in high net to gross fluvial reservoirs upon oil recovery was addressed by Atkinson *et al.,* (1990) in the Ivishak Formation, the main reservoir in the Prudhoe Bay field, Alaska. This showed that heterogeneously distributed permeabilities in braided deposits, where significant amounts of conglomerates and conglomeratic sandstone deposits occur along with shaly intervals, hinders effective and homogeneous oil production through the less permeable intervals found in the reservoir, the OFC having the main producing intervals with the greatest flow

and injection rates. Gershenzon *et al.,* (2015) based on flow simulations in the Ivishak Formation in the Prudhoe Bay oilfield, Alaska, showed that the recovery efficiency was greater when the amount of OFC was lower and the pressure gradient between injectors and producers was oriented perpendicular to the direction of the OFC. As the flow simulations in the Castissent models advanced, a gradual slowdown in the waterfront displacement within each channel of Complex A was observed in both Models 1 and 2. This effect was due to the upward decrease in porosity and permeability values, which enhances segregation of the injected fluids and favours flow in the bottom of the succession (Fig. 14).

Thick fining-upwards successions, like the sandy braided deposits of A1 or the coarse-grained meandering deposits of A3, are also reported by Bailey *et al*., (2000) to enhance a water-flow segregation towards the bottom of the packages, mainly because of the viscosity contrasts and gravity effects. This effect is also documented by Cabello *et al.,* (2018) in point-bar deposits of the Montllobat Formation, Spain, where the waterfront preferentially ascends through the accretion deposits and progressive permeability contrasts occur. However, the upwards decrease in the reservoir quality and gravity effects prevent the oil from being completely drained from the upper part of the point bar.

At the end of the simulations, the presence of the thief zones, the vertical segregation of the flow and the permeability barriers, resulted in bypassed oil accumulations in the models. The poorly swept areas tend to form two vertically stacked oil accumulations, 5–10 m thick, between the injector wells. These non-swept oil zones are located in the upper part of the unit-bars and dunes of A1 and in the upper part of the gravel bars, scour and fill deposits, and dunes interval up to the accretionary bank of A3, i.e., immediately below the impermeable units corresponding to both the mud-clast channel lag and the floodplain mudstones (Fig. 14).

8.2 Trapped oil and petrophysical heterogeneity

The recovery efficiency reported in the simulation of Model 1 is less than 1% below the recovery efficiency obtained for Model 2 (i.e., 50.41% and 50.58%, respectively). The percentage of trapped moveable oil in both models is also very similar (35.38% and 34.79% in Models 1 and 2, respectively).

Later water breakthroughs and more gradual increase of the water cut through time in Model 1 (Fig. 13) suggests that the heterogeneity associated with the petrophysical property distribution significantly affects the water and the oil displacement in the reservoir during production. In Model 1, with constant petrophysical values, the water front advances more homogeneously through each of the modelled intervals than in Model 2 (Fig. 14). This favours a more gradual water production (Fig. 13).

The increase in the sedimentary and petrophysical heterogeneity captured in Model 2 decreased the oil trapping efficiency of the coarser-grained intervals in Complex A (i.e., the channel lag and the lower unit-bars in A1, the unit-bars and dunes interval of A2) (Fig. 15). The fingering effects and effectivity of the thief zones during production was enhanced in Model 2, catching most of the injected water. The productivity in the intervals immediately above the coarser-grained units (i.e., the dunes and upper unit-bars of A1, and the transverse bars and accretionary bank in A3) was reduced (Fig. 15). This was in part because of the increase in the efficiency of the thief zones, but also as a response to the reduction in porosity and permeability caused by the fining-upwards trend captured in Model 2, which caused a progressive decay in the productivity of the waterfront towards the upper sections of the channel belts (Fig. 14).

The results obtained from this case study can guide the reservoir modelling process and the understanding of hydrocarbon production in gravel-sandstone dominated channel-belt deposits, where a wide range of grain sizes is present. The proportion of gravel and sandstone, the fining-upwards trends, and the presence of shale barriers are all key to building a robust model. A robust development and a well placement strategy must be built, based on the prediction of the impact of the sedimentary heterogeneities over the fluid-flow behaviour and the location of the oil accumulations that will be bypassed.

9. Conclusions

The characterisation of the fluvial sandstone Complex A of the Castissent Formation in the Mas de Faro outcrop allow us to conclude the following:

- The results from the facies analysis show a fining-upwards trend, starting with a basal gravel lag, of unit-bar and dune deposits for A1, a mud-clast channel lag passing to unit-bar and dune deposits for A2, and a fining-upwards succession in A3, starting with scour-and-fill, gravel bars and dune deposits passing upwards to transverse bar deposits and ending in mottled accretionary bank deposits composed of small dunes, plane beds and rippled sands which is capped by floodplain deposits.
- Each channel belt exposes a single-story, interpreting a channel-fill or downstream-accreting story (i.e., a compound bar), associated with sandy braided rivers, for A1 and A2 and a laterally-accreting story (i.e., a point bar), associated with coarse-grained meandering-rivers, for A3.

- The gravel channel lag at the base of the sandstone Complex A, the unit-bar deposits of A1 and A2, and the gravel bars, scour-and-fill and dune deposits at the base of A3, acted as thief zones that caught a great part of the injected water producing fingering of the waterfront and caused early water breakthrough.
- Upwards-fining successions produced a slowdown and non-synchronous displacement of the waterfront, reducing the sweeping efficiency of the upper parts of the channel belts. This effect is mainly related to the gradual decrease in porosity and permeability values, which enhanced segregation of the injected fluids towards the bottom of the successions.
- The remaining oil is located at the midpoint between the injector wells, where there are two vertically stacked accumulations, isolated from water sweeping since the fluids are circulating through the underlying, more permeable zones.
- The increase in the degree of petrophysical and sedimentary heterogeneity favours a decrease in the amount of oil trapped for the coarser-grained intervals and enhances the trapping efficiency for the finer-grained intervals; in contrast, the decrease of the heterogeneity degree offsets the effects of the thief zones and the fingering effects and promotes more balanced production.
- We have demonstrated that the sedimentary heterogeneity related to the presence of thief zones, fining-upwards trends and mud-rich intervals in amalgamated gravel-sandy dominated multi-storey fluvial successions has an important control on the fluid-flow behaviour and drastically impacts the reservoir productivity and recovery efficiency, trapping 35.38% and 34.79% of the OOIP in each simulation.

Acknowledgments

Thanks, are given to Schlumberger for the donation of the Petrel E&P licenses, to the Virtual Outcrop Geology Group for the donation of LIME licenses, to Petroleum Experts for the donation of MOVE licenses, to Innovmetric for the donation of the Polyworks license and to Agisoft for the donation of the Agisoft Photoscan license. Magda Chmielewska is acknowledged for the technical support during the virtual outcrop processing. Support from the Ministerio de Economía y Competitividad (Project SEROS CGL2014-55900-P) and from the Generalitat de Catalunya (2017SGR596) is gratefully acknowledged. Thanks to reviewers Brian Willis and César Viseras and also to the Associate Editor Luca Colombera for their constructive comments, which have improved the content of this paper.

References

Ashworth, P.J., Sambrook, G.H., Best, J.L., Bridge, J.S., Lane, S.N., Lunt, I.A., Reesink, A.J.H., Simpson, C.J. and Thomas, R.E. (2011): Evolution and sedimentology of a channel fill in the sandy braided South Saskatchewan River and its comparison to the deposits of an adjacent compound bar. *Sedimentology*, V.58, p.1860-1883. http://doi.org/10.1111/j.1365-3091.2011.01242.x

Atkinson, C.C., McGowen, J.H., Bloch, S., Lundell, L.L. and Trumbly, P.N. (1990). Braidplain and deltaic reservoir, Prudhoe Bay Field, Alaska. *Sandstone Petroleum Reservoirs,* p.7-29. http://doi.org/10.1007/978-1-4613-8988-0_2

Bailey, B., Crabtree, M., Tyrie, J., Elphick, J., Kuchuk, F., Romano, C. and Roodhart, L. (2000): Water Control. *Oilfield Review Schlumberger,* p.30-51.

Benson, G.S. (2015): Estimation of Arithmetic Permeability from a Semi-Log Porosity/Log10 Permeability Regression. *AAPG Search and Discovery.*

Bluck, B.J. (1971): Sedimentation in the meandering River Endrick. *Scottish Journal of Geology*, V. 7, p. 93–138. https://doi.org/10.1144/sjg07020093.

Bridge, J.S. (2001): Characterization of fluvial hydrocarbon reservoirs and aquifers: problems and solutions. *Revista de la Asociación Argentina de Sedimentología*, V. 8, No.2, p. 87-114.

Buckley, S.J., Ringdal, K., Naumann, N., Dolva,B., Kurz, T.H., Howell, J.A. and Dewez, T.J.B, in review 2018: LIME: 3D visualization, interpretation and communication of virtual geoscience models. *Geosphere.*

Cabello, P., Domínguez, P., Murillo-López, M.H., López-Blanco, M., García-Selles, D., Cuevas, J.L., Marzo, M. and Arbués, P. (2018): From conventional outcrop datasets and digital outcrop models to flow simulation in the Pont de Montanyana point-bar deposits (Ypresian, Southern Pyrenees). *Marine and Petroleum Geology,* V.18, p.19-42. https://doi.org/10.1016/j.marpetgeo.2018.03.040

Cámara, P. and Klimowitz, J. (1985): Interpretación geodinámica de la vertiente centro-occidental surpirenaica (Cuencas de Jaca-Tremp). *Estudios Geológicos*, V. 41, p. 391-404. https://doi.org/10.19389/egeo l.85415-6720.

Campbell, C.V. (1967): Lamina, lamina-set, bed and bedset. *Sedimentology*, V. 8, p.7-26. https://doi.org/10.1111/sed.1967.8.issue-1

Chesley, J.T., Leier, A.L., White, S. and Torres, R. (2017): Using unmanned aerial vehicles and structure-from-motion photogrammetry to characterize sedimentary outcrops: An example from the Morrison Formation, Utah, USA. *Sedimentary Geology,* V.354, p.1-8.

Collinson, J.D. (1969): The sedimentology of the Grindslow shales and the Kinderscout grit; a deltaic complex in the Namurian of northern England. Journal of Sedimentary Research, V.39, No.1, p.194-221. https://doi.org/10.1306/74D71C17-2B21-11D7-8648000102C1865D

Collinson, J.D. (1970): Bedforms of the Tana River, Norway. *Geografiska Annaler: Series A, Physical Geography*, V. 52, No. 1, p. 31-56.

Deutsch, C. V. and Journel, A. G. (1997): GSLIB: Geostatistical Software Library and User's Guide, 2nd ed. Oxford University Press, New York, 368 pp.

Eden Van, J.G. (1970): A reconnaissance of deltaic environment in the middle Eocene of the South-Central Pyrenees, Spain. –*Geol. Mijnb.*, V. 49, p. 145–157.

Falivene, O., Cabrera, L., Muñoz, J.A., Arbués, P., Fernández, O. and Sáez, A. (2007): Statistical grid-based facies reconstruction and modelling for sedimentary bodies. Alluvial-palustrine and turbiditic examples. Geol. Acta V. 5, p. 199–230. http://dx.doi. org/10.1344/105.000000295.

Ford, G.L. and Pyles, D.F. (2014): A hierarchical approach for evaluating fluvial systems: Architectural analysis and sequential evolution of the high net-sand content, middle Wasatch Formation, Uinta Basin, Utah. *AAPG Bulletin*, V.98, p.1273-1304. https://doi.org/ 10.1306/12171313052

Friend, P.F., Slater, M.J. and Williams, R.C. (1979). Vertical and lateral building of river sandstone bodies. Ebro Basin, Spain. *J. Geol. Soc. London,* V.136, p.39-46.

Garzanti, E. (1991): Non-carbonate intrabasinal grains in arenites: their recognition, significance, and relationship to eustatic cycles and tectonic setting. *Journal of Sedimentary Petrology,* V.61, p.959-975.

Gershenzon, N.I., Soltanian, M., Ritzi, R.W. and Dominic, D.F. (2015): Understanding the impact of open-framework conglomerates on water-oil displacements: the Victor interval of the Ivishak Reservoir, Prudhose Bay Field, Alaska. *Petroleum Geoscience,* V.21, No. 1, p.43-54. https://doi.org/10.1144/petgeo2014-017

Henares, S., Arribas, J., Cultrone, G. and Viseras, C. (2016): Muddy and dolomitic rip-up clasts in Triassic fluvial sandstone: origin and impact on potential reservoir properties (Argana Basin, Morocco). *Sedimentary Geology*, V. 339, p.218-233. https://doi.org/10.1016/j.sedgeo.2016.03.020

Howell, J.A., Martinius, A.W. and Good, T.R. (2014): The application of outcrop analogues in geological modelling: a review, present status and future outlook. *Geol. Soc., London, Spec. Publ.,* V. 387, p. 1- 25. https://doi.org/10.1144/SP387.12

Høimyr, Ø., Kleppe, A. and Nystuen, J.P. (1993): Effect of heterogeneities in a braided stream channel sandbody on simulation of oil recovery: a case study from the Lower Jurassic Statfjord Formation, Snorre Field, North Sea. In: M. Ashton (editor*) Advances in Reservoir Geology. Geol. Soc., London, Spec. Publ*., V. 69, p. 105–134. https://doi.org/10.1144/GSL.SP.1993.069.01.06.

Instituto Geográfico Nacional. (2013). Base Topográfica BTN25, Hoja 289. Ellipsoide SGR80, Universal Transverse Mercator, Datum ETRS89.

Jones, J.A. and Hartley, A.J. (1993): Reservoir characteristics of a braid-plain depositional system: The Upper Carboniferous Pennant Sandstone of South Wales. *Geological Society of London Special Publications, V. 73, p. 143- 156.* https://doi.org/10.1144/GSL.SP.1993.073.01.09.

Keogh, K. J., Leary, S., Martinius, A. W., Scott, A. S. J., Riordan, S., Viste, I., Gowland, S., Taylor, A. M. and Howell, J. (2014): Data capture for multiscale modelling of the Lourinhã Formation, Lusitanian Basin, Portugal: an outcrop analogue for the Statfjord Group, Norwegian North Sea. In: Martinius, A. W., Howell, J.A. & Wood, T. R. (eds) *Sediment-Body Geometry and Heterogeneity: Analogue Studies for Modelling the Subsurface, Geol. Soc., London, Spec. Publ*., V. 387, p. 27–56. https://doi.org/10.1144/SP387.11.

Lia, O., Tjelmeland, H. and Kjellesvik, L.E. (1996): Modeling of facies architecture by marked point models. In: Fifth International Geostatistics Congress, Wollongong, Australia. Kluver Academic Publishers, Proceedings, pp. 386–398.

Lunt, I.A., Bridge, J.S. and Tye, R.S. (2004): A quantitative, three-dimensional depositional model of gravelly braided rivers. *Sedimentology,* V.51, p.377-414. https://doi.org/10.1111/j.1365-3091.2004.00627.x

Marzo, M., Nijman, W. and Puigdefàbregas, C. (1988): Architecture of the Castissent fluvial sheet sandstones, Eocene, south Pyrenees, Spain. *Sedimentology*, V. 35, p. 719-738. https://doi.org/10.1111/j. 1365-3091.1988.tb01247.x.

McGowen, J.H. and Garner, L.E. (1970): Physiographic features and stratification types of coarse-grained point bars: modern and ancient examples. *Sedimentology*, V. 14, p. 77-111. https://doi.org/10.1111/j.1365-3091.1970.tb00184.x.

Miall, A.D. (1988): Reservoir heterogeneities in fluvial sandstones: Lessons from outcrop studies. *The American Association of Petroleum Geologists Bulletin*, V. 72, No.6, p. 682-697. https://doi.org/10.1306/703C8F01-1707-11D7-8645000102C1865D.

Miall, A.D. (1985): Architectural element analysis: A new method of facies analysis applied to fluvial deposits. Earth-Science Reviews, V.22, No. 4, p. 261-308. https://doi.org/10.1016/0012-8252(85)90001-7

Miall, A.D. (1978): Lithofacies types and vertical profile models in braided river deposits: a summary. In: A.D. Miall (editor) *Fluvial Sedimentology. Can. Soc. Petrol. Geol. Mem.,* V. 5, p.597-604.

Miall, A.D. (1977): A review of the braided river depositional environment. *Earth-Science Reviews*, V. 13, p. 1–62. https://doi.org/10.1016/0012-8252(77)90055-1.

Muñoz, J.A. (2002): Fault related folds in the southern Pyrenees. In: *AAPG Bulletin*, V.101, No.4 (April 2017), p. 579–587. https://doi.org/10.1306/011817DIG17037.

Muñoz, J.A., McClary, K. and Poblet, J. (1994): Synchronous extension and contraction in frontal thrust sheets of the Spanish Pyrenees. *Geology*, V. 22, p. 921–924. https://doi.org/10.1130/0091-7613(1994)022<0921:SEACIF>2.3.CO;2.

Muñoz, J.A. (1992): Evolution of a continental collision belt: ECORS-Pyrenees crustal balanced cross-section. In: K.R.McClay, (editor) *Thrust tectonics*: London, Chapman & Hall, p. 235–246. https://doi.org/10.1007/978-94-011-3066-0_21.

Nijman, W. (1998): Cyclicity and basin axis shift in a piggyback basin: towards modelling of the Eocene Tremp-Ager Basin, South Pyrenees, Spain. In*:* Mascle, A., Puigdefàbregas, C., Luterbacher, H.P. & Fernàndez, M. (eds) *Cenozoic Foreland Basins of Western Europe*. *Geological Society Special Publications*, V. 134, p. 135–162. https://doi.org/10.1144/GSL.SP.1998.134.01.07.

Nijman, W. and Puigdefàbregas, C. (1978): Coarse-grained point bar structure in a molasse-type system, Eocene Castissent Sandstone Formation, South Pyrenean Basin. In: A.D. Miall (editor), *Fluvial Sedimentology*. *Mem. Can. Soc. Petrel. Geol.*, V. 5, p. 487–510. https://doi.org/10.1111/j.1365-3091.1988.tb01247.x.

Nijman, W. and Nio. S.D. (1975): The Eocene Montañana Delta, Tremp-Graus Basin, Southern Pyrenees. In: J. Rosell & C. Puigdefàbregas (eds) *Sedimentary Evolution of the Palaeogene South Pyrenean Basin, Excursion 19* . IXth. Int. Sed, Congre., Nice, France, 56 pp.

Nordhal, K. and Ringrose, P.S. (2008): Identifying the representative elementary volume for permeability in heterolithic deposits using numerical rock models. *Mathematical Geosciences*. V. 40, No. 7, p. 753-771.

North, C.P. and Taylor, K.S. (1996): Ephemeral-fluvial deposits: Integrated outcrop and simulation studies reveal complexity. *American Association of Petroleum Geologists*, *Bulletin*, V. 80, p. 811-830.

Norwegian Petroleum Directorate (2016). Open Source Online Resources: FactMaps and FactPages.

Puigdefàbregas, C., Muñoz, J.A. and Vergés,J. (1992): Thrusting and foreland basin evolution in the southern Pyrenees. In: McClary, K.R., (editor) *Thrust tectonics*: London, Chapman and Hall, p. 247–254.

Reesink, A.J.H. and Bridge, J.S (2007): Influence of superimposed bedforms and flow unsteadiness on formation of cross strata in dunes and unit bars. *Sedimentary Geology*, V.202, p.281-296. https://doi.org/10.1016/j.sedgeo.2007.02.005

Reesink, A.J.H. and Bridge, J.S (2011): Evidence of bedform superimposition and flow unsteadiness in unit-bar deposits, South Saskatchewan River, Canada. *Journal of Sedimentary Research*, V.81, p.814-840. https://doi.org/10.2110/jsr.2011.69

Ringrose, P.S. and Bentley, M. (2015): Reservoir Model Design: A Practitioner's Guide. Springer, Dordrecht Heidelberg New York London.

Ryseth, A. (2001): Sedimentology and palaeogeography of the Statfjord Formation (Rhaetian-Sinemurian), North Sea. In: O.J. Martinsen & T. Dreyer (eds) *Sedimentary Environments offshore Norway – Palaeozoic to Recent, Norw. Petrol. Soc. Spec. Publ.,* V. 10, p. 67–85.

Ryseth, A. and Ramm, M. (1996): Alluvial architecture and differential subsidence in the Statfjord Formation, North Sea: prediction of reservoir potential. *Petroleum Geoscience*, V. 2, p. 271-287. https://doi.org/10.1144/petgeo.2.3.271.

Saura, E., Ardèvol i Oro, Ll., Teixell, A. and Vergés, J. (2016): Rising and falling diapirs, shifting depocenters, and flap overturning in the Cretaceous Sopeira and Sant Gervàs subbasins (Ribagorça Basin, southern Pyrenees). *Tectonics,* V. 35, p. 638–662. https://doi.org/10.1002/2015TC004001.

Séguret, M. (1972): Étude tectonique des nappes et series décollées de la partie centrale du versant sud des Pyrénées-Charactère synsedimentaire, role de la comprensión et de la gravité: Montpellier, France. *Publications Université des Sciences et Techniques du Languedoc*, Série Géologie Structurale 2, 155 pp.

Timur, A. (1968): An investigation of permeability, porosity and residual water saturation relationship for sandstone reservoirs. *The Log Analyst*, V.9, No. 4, 8 pp.

Tyler, N. and Findley, R.J. (1991): Architectural controls on the recovery of hydrocarbons from sandstone reservoirs, in: Miall, A.D., Tyler, N. (Eds.), The Three-dimensional Facies Architecture of Terrigenous Clastic Sediments and Its Implications for Hydrocarbon Discovery and Recovery. Concepts in Sedimentology and Palaeontology. Society for Sedimentary Geology, Tulsa, p. 1–5.

Vergés, J. and Muñoz, J.A. (1990): Thrust sequences in the southern central Pyrenees. *Bull. Soc. Géol. France*, V. 6, No. 2, p. 265–271. https://doi.org/10.1016/0191-8141(85)90111-7.

Viseras, C., Fernández, J., García-García, F., Soria, J.M., Calvache, M.L. and Jáuregui, P. (2009): Dynamics of sedimentary environments in the accelerated siltation of a reservoir: the case of Alhama de Granada, southern Spain. *Environmental Geology*, V. 56, p.1353-1369. https://doi.org/10.1007/s00254-008-1231-2

Viseras, C., Soria, J.M., Durán, J.J., Pla, S., Garrido, G., García-García, F. and Arribas, A. (2006): A large-mammal site in a meandering fluvial context (Fonelas P-1, Late Pliocene, Guadix Basin, Spain). Sedimentological keys for its paleoenvironmental reconstruction. *Palaeogeography, Palaeoclimatology, Palaeoecology*, V. 242, p.139-168. https://doi.org/10.1016/j.palaeo.2006.05.013

FIGURE CAPTIONS

Figure 1. Geological map of the northeast of the Iberian Peninsula. The Tremp-Graus Basin is located on top of the Montsec thrust sheet, forming an ESE-WNW syncline. The white star shows the location of the Mas de Faro outcrop within the Tremp-Graus Basin. Modified from Muñoz (2002) and Cabello *et al.,* (2018).

Figure 2. Cross-section of the Montanyana Group in the Tremp-Graus Basin. The Castissent Formation represents a strong progradation of the depositional systems towards the northwest and separates the upper from the lower Montanyana Sub-Group. The black star marks the position of the Mas de Faro outcrop. Modified from Nijman and Puigdefàbregas (1978).

Figure 3. A) Location of the Mas de Faro outcrop and position of the stratigraphic logs. B and C) Images from the virtual outcrop, which show the general physiography and exposures of the Castissent Formation at the Mas de Faro area. Topographic map and orthophoto modified from IGN (2013). D) Summarized stratigraphic profile of the Castissent Formation with the main fluvial bodies that form the Complex A and their boundaries. Modified from Marzo *et al.,* (1988).

Figure 4. Photographs of the facies described in Table 1. A) Pebble-cobble conglomerates (Gm). B-C) Planar-asymptotic cross-stratified unit-bar deposits (Sp1), note the fining-upwards tendency. D) Dune deposits (St1). E) Mud-clast channel lag with variable amounts of pebbles (Mcgl). F-G) Gravel bars, scour-and-fill and dune deposits (Gt, Gp and St1). H) Planar-asymptotic cross-stratified transverse bars (Sp2). I) Mottled medium-to-fine trough and horizontally bedded sandstones (St2 and Sh). J) Asymmetrical current ripples (Sr).

Figure 5. Sedimentary architecture and stratigraphic intervals modelled along the fluvial succession of Complex A in the Mas de Faro area. See Fig. 3B for image location. The traced lines correspond to the reconstructed horizons during the 3D modelling in Petrel, except for the lateral-accretion surfaces of A2 and the dune interval of A2. See Fig. 10A.

Figure 6. Type log for the Mas de Faro area, which summarizes the different features observed trough the 9 stratigraphic logs made, along with the porosity log derived from the regressions of the petrophysical values. Note the fining-upwards tendencies in A1, A2 and A3 channel-belt deposits, and the progressive migration of the palaeocurrents towards the west-southwest.

Figure 7. Palaeocurrent maps for the different stratigraphic intervals studied. Dip marks represent the mean value of the palaeocurrents direction measured for a given interval at the different logs. See Fig. 6 for rose diagrams. Solid black lines represent the base of A1, A2 and A3.

Figure 8. Eiriksson Formation well data. A) Map showing the location of the wells that penetrated the Eiriksson Formation in the North Sea and that were used to derive the petrophysical values used in the modelling of Castissent Complex A (see Fig. 9). Modified from Keogh *et al.,* (2014) and Norwegian Petroleum Directorate (2016). B) Stratigraphic log and porosity log from the petrophysical analysis of the Eiriksson Formation. Modified from Ryseth and Ramm (1996).

Figure 9. Petrophysical property regressions in the Eiriksson Formation. The resulting relationships were used to relate the grain size in Castissent Complex A with the different rock properties, and to construct the relative permeability functions used in the flow simulation (see Fig. 12).

Figure 10. A) 2D section showing the different zones modelled and the layering applied. Vertical exaggeration x1. B) Horizons modelled. Vertical exaggeration x4. C) Detail of the gravel channel lag zone, which was modelled as an object within a sand background. Vertical exaggeration x4.

Figure 11. Interpreted deposits, porosity and permeability XY-Z 3D geocellular models. The left row corresponds to Model 1, assigned with average and constant values for each zone, while Model 2, right row, was built using the SGS algorithm and shows a higher degree of heterogeneity. Vertical exaggeration x4.

Figure 12. Permeability functions for the Castissent Formation. The upper image corresponds to Model 1, which is a simple model that records a lower degree of petrophysical heterogeneity than Model 2, below, which takes into account higher permeability contrasts. The permeability curves in Model 2 were defined on the basis of the porosity, creating a permeability curve for each 1% change in porosity. For porosity values between 15 and 5%, the same permeability function was used. For values equal or lower to 5% no permeability function was used since they were treated as relatively impermeable facies.

Figure 13. Reservoir performance at the end of the flow simulations. Curves correspond to the recovery efficiency and water cut for both simulation cases plotted against the IPV. Note that the increase in water cut and recovery efficiency curves for Model 1 is more progressive than in Model 2. One realization for each model.

Figure 14. Different stages during the run of the flow simulation for both models. Note the fingering located at the base of the channels and the slowdown in the waterfront displacement during the early stages of the simulation. Note the compartmentalization of the reservoir analogue due to the relatively impermeable mud-clast channel lag at the base of A2 and the location of the bypassed oil accumulations. Vertical exaggeration x4.

Figure 15. Oil trapping efficiency. Percentage of moveable oil trapped respect to the OOIP in each interval at the end of the simulations. Note that most of the coarse-grained intervals in Model 2 tend to trap a minor amount of oil whereas the finer-grained facies and the intervals immediately above the thief zones tend to trap a greater amount of oil compared to Model 1, where a more balanced contribution is shown.

Table 1. Compilation of the different facies described and interpreted along the fluvial succession of Complex A in the Mas de Faro outcrop.

Table 2. Compilation of the different types of story and interpreted forms.

Table 3. Input data for the facies and petrophysical models. For each interval modelled the type of algorithm used and the corresponding values are shown. Model 1 was built using average values while in Model 2 variogram

analysis were conducted in order to model a higher degree of petrophysical variability within the Mas de Faro outcrop.

Figure 1

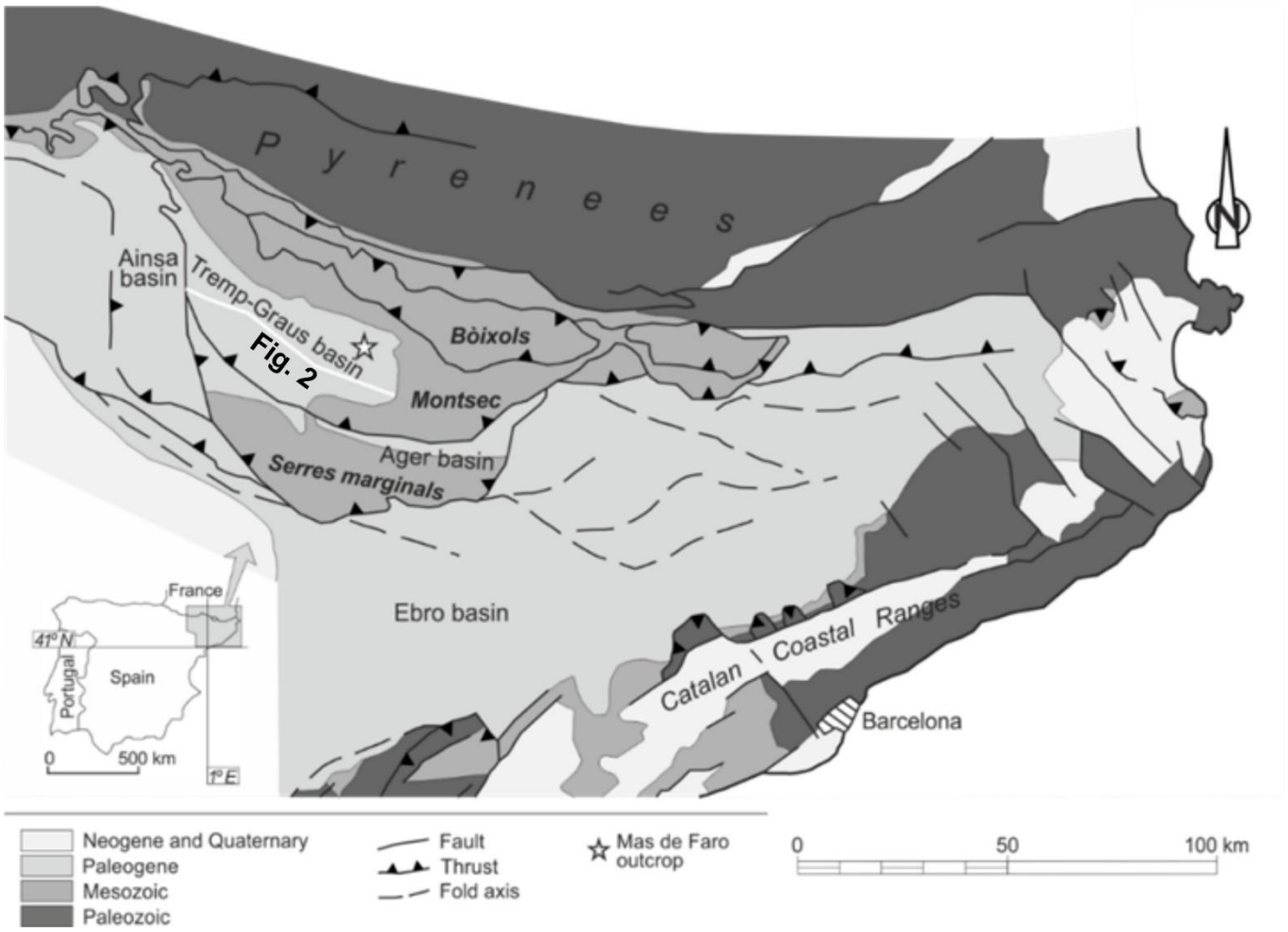

Figure 2

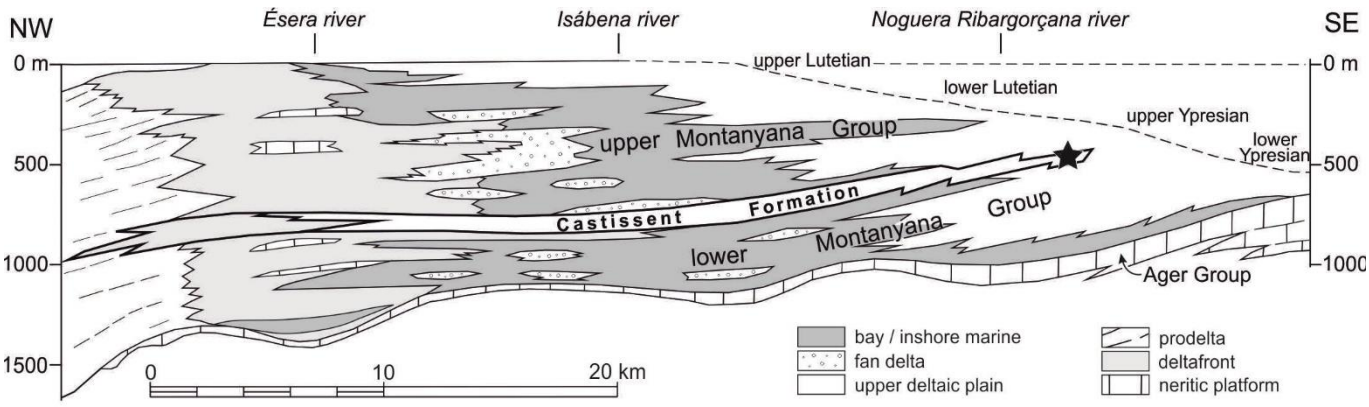

Figure 3

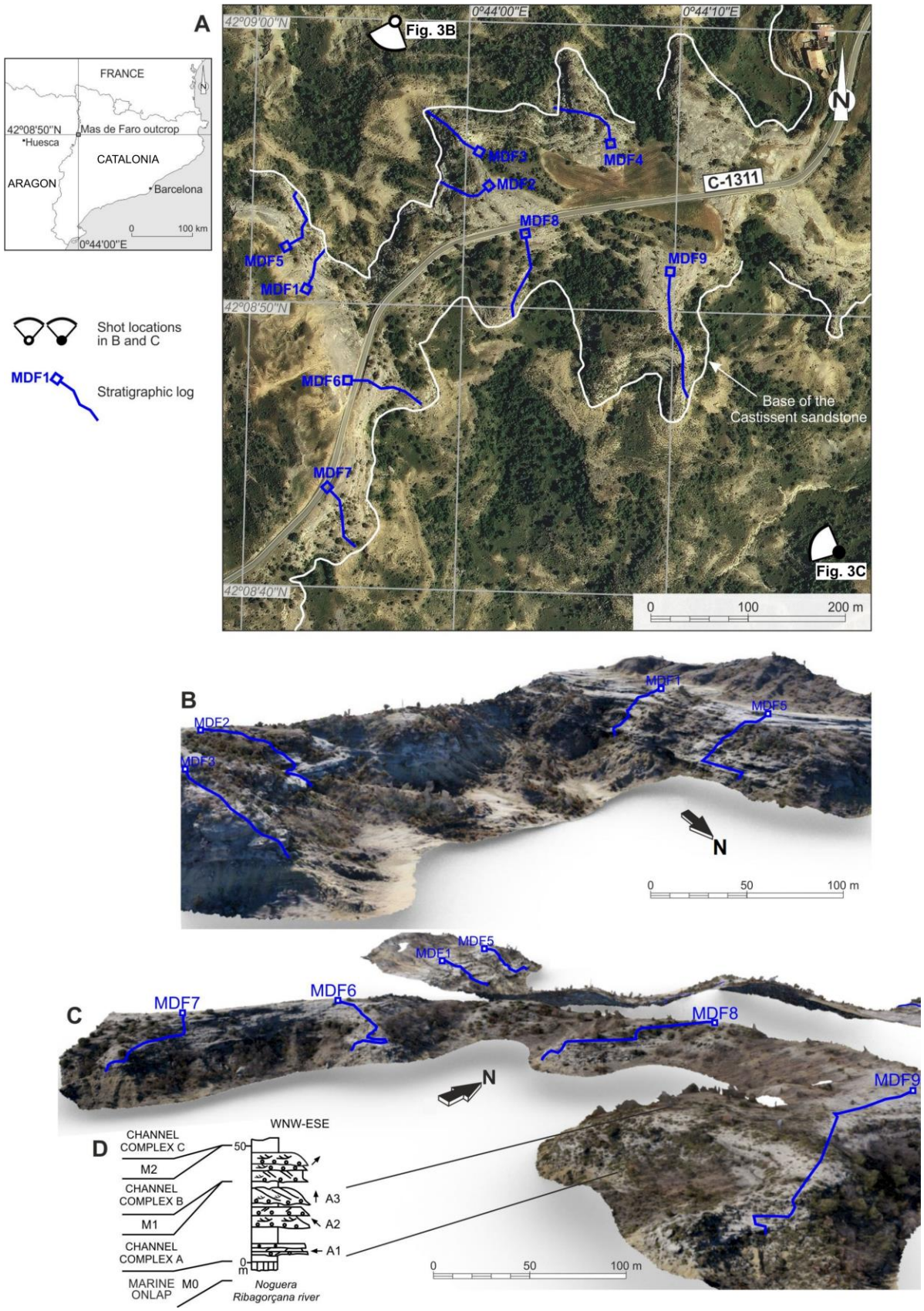
A
FRANCE
42º08'50"N
Mas de Faro outcrop
Huesca
CATALONIA
ARAGON
Barcelona
0
100 km
0º44'00"E
Shot locations in B and C
MDF1
Stratigraphic log
42º09'00"N
Fig. 3B
0º44'00"E
0º44'10"E
N
MDF3
MDF4
MDF2
C-1311
MDF8
MDF5
MDF1
MDF9
42º08'50"N
MDF6
Base of the Castissent sandstone
MDF7
Fig. 3C
42º08'40"N
0
100
200 m
B
MDF2
MDF3
MDF1
MDF5
N
0
50
100 m
C
MDF7
MDF6
MDF5
MDF1
MDF8
MDF9
N
0
50
100 m
D
WNW-ESE
CHANNEL COMPLEX C
M2
CHANNEL COMPLEX B
M1
CHANNEL COMPLEX A
MARINE ONLAP
M0
50
0
m
A3
A2
A1
Noguera Ribagorçana river

Figure 4

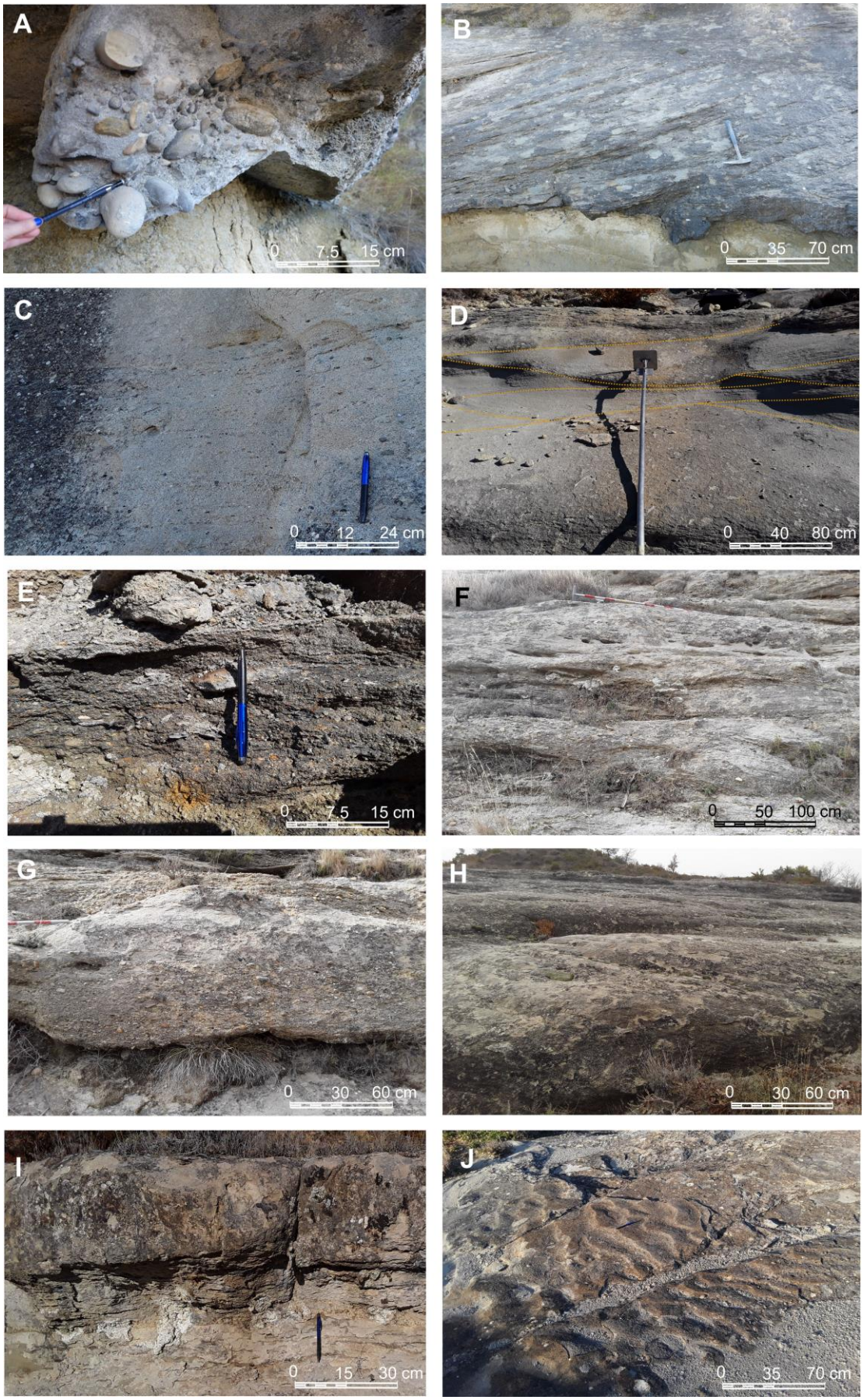
A
0 7.5 15 cm
B
0 35 70 cm
C
0 12 24 cm
D
0 40 80 cm
E
0 7.5 15 cm
F
0 50 100 cm
G
0 30 60 cm
H
0 30 60 cm
I
0 15 30 cm
J
0 35 70 cm

Figure 5

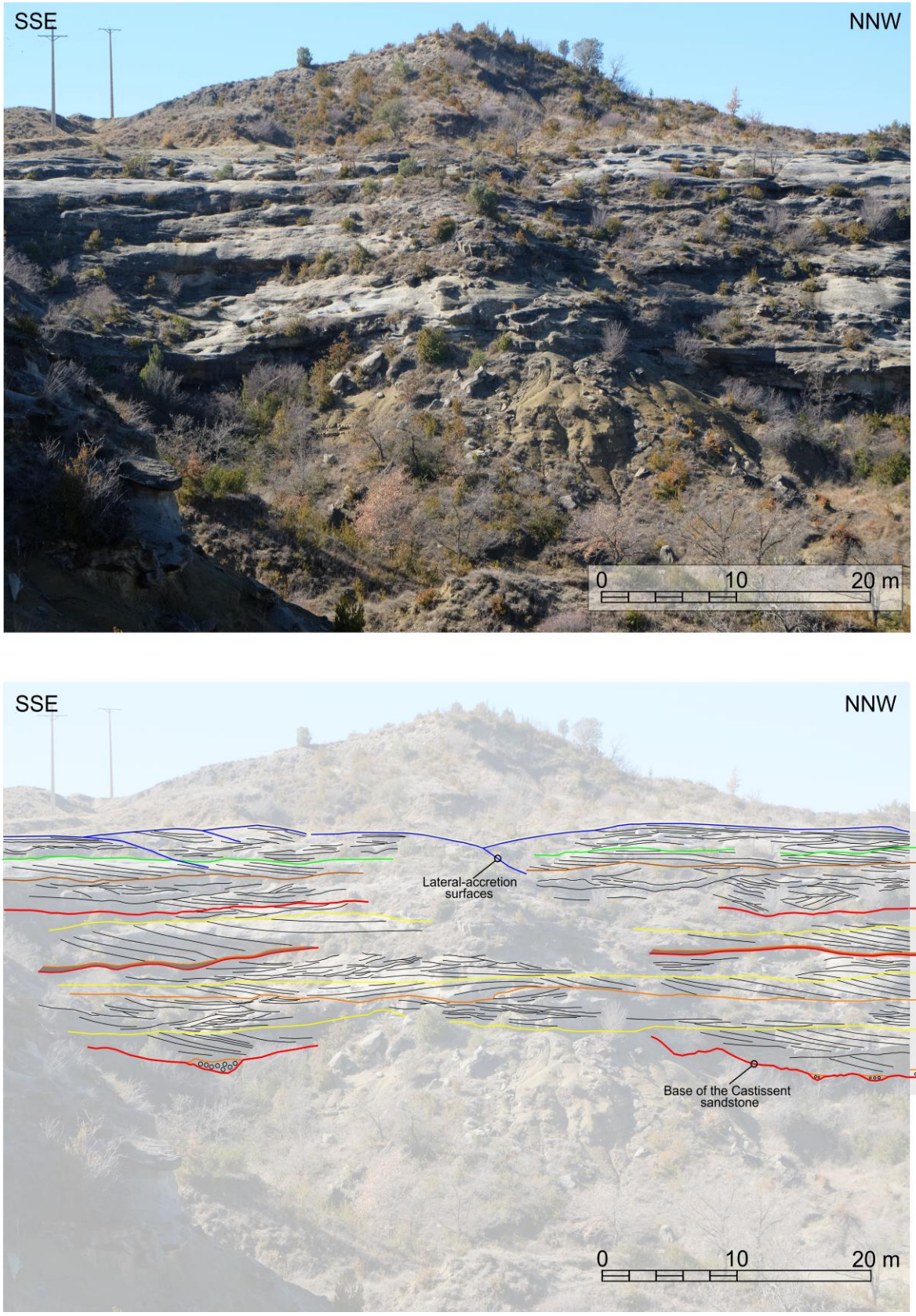
SSE
NNW
0
10
20 m
SSE
NNW
Lateral-accretion surfaces
Base of the Castissent sandstone
Floodplain
Accre. bank
Transverse bars
Gravel bars, scour-and-fill deposits and dunes
A3
Dunes
Unit-bars
A2
Mud-clast lag
Dunes
Unit-bars
Dunes
A1
Unit-bars
Gravel lag
Floodplain
0
10
20 m

Figure 6

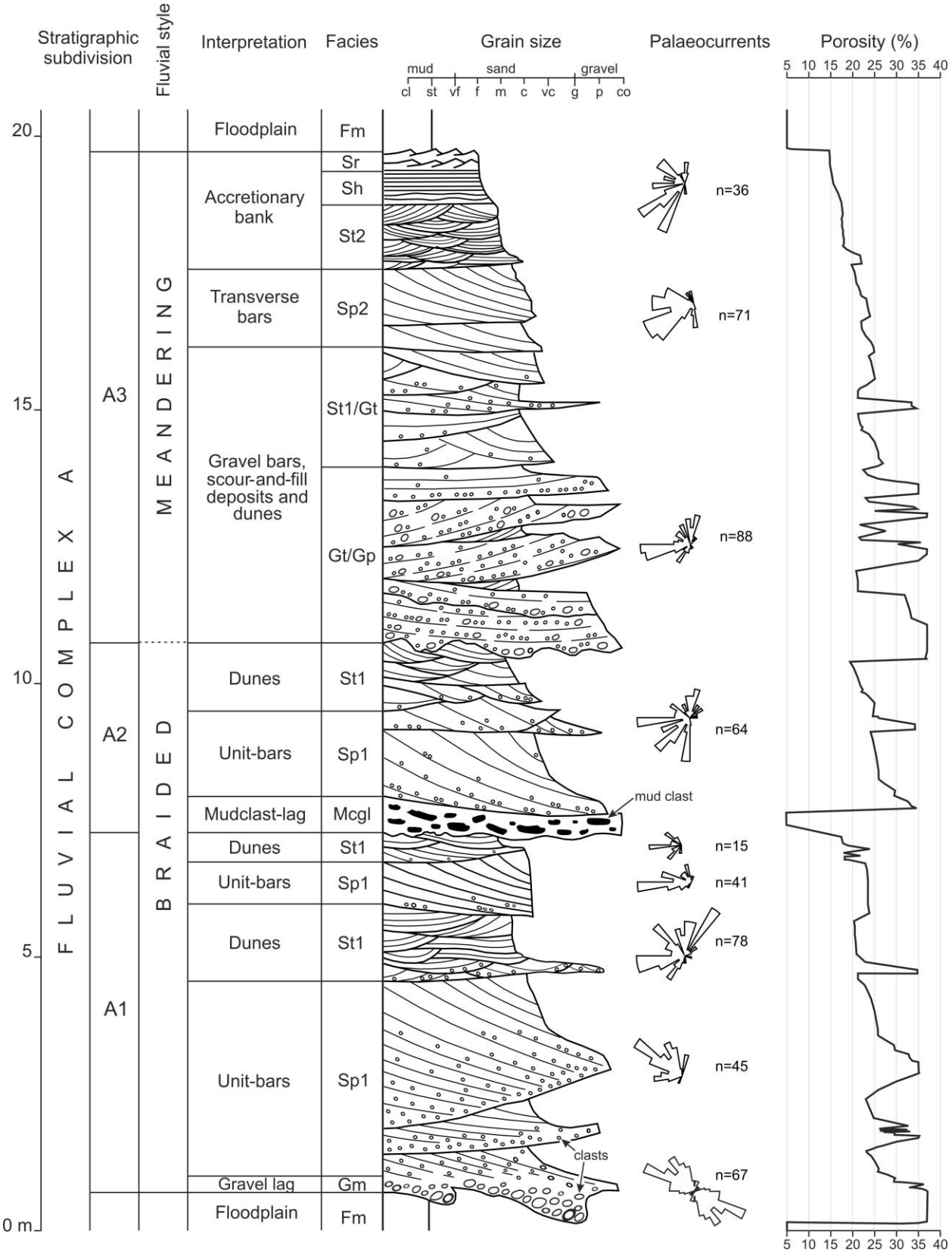
Stratigraphic subdivision
Fluvial style
Interpretation
Facies
Grain size
mud
sand
gravel
cl st vf f m c vc g p co
Palaeocurrents
Porosity (%)
5 10 15 20 25 30 35 40
20
15
10
5
0 m
FLUVIAL COMPLEX A
A3
A2
A1
MEANDERING
BRAIDED
Floodplain
Fm
Sr
Sh
St2
Accretionary bank
Transverse bars
Sp2
St1/Gt
Gravel bars, scour-and-fill deposits and dunes
Gt/Gp
Dunes
St1
Unit-bars
Sp1
Mudclast-lag
Mcgl
Dunes
St1
Unit-bars
Sp1
Dunes
St1
Unit-bars
Sp1
Gravel lag
Gm
Floodplain
Fm
mud clast
clasts
n=36
n=71
n=88
n=64
n=15
n=41
n=78
n=45
n=67
5 10 15 20 25 30 35 40

Figure 7A

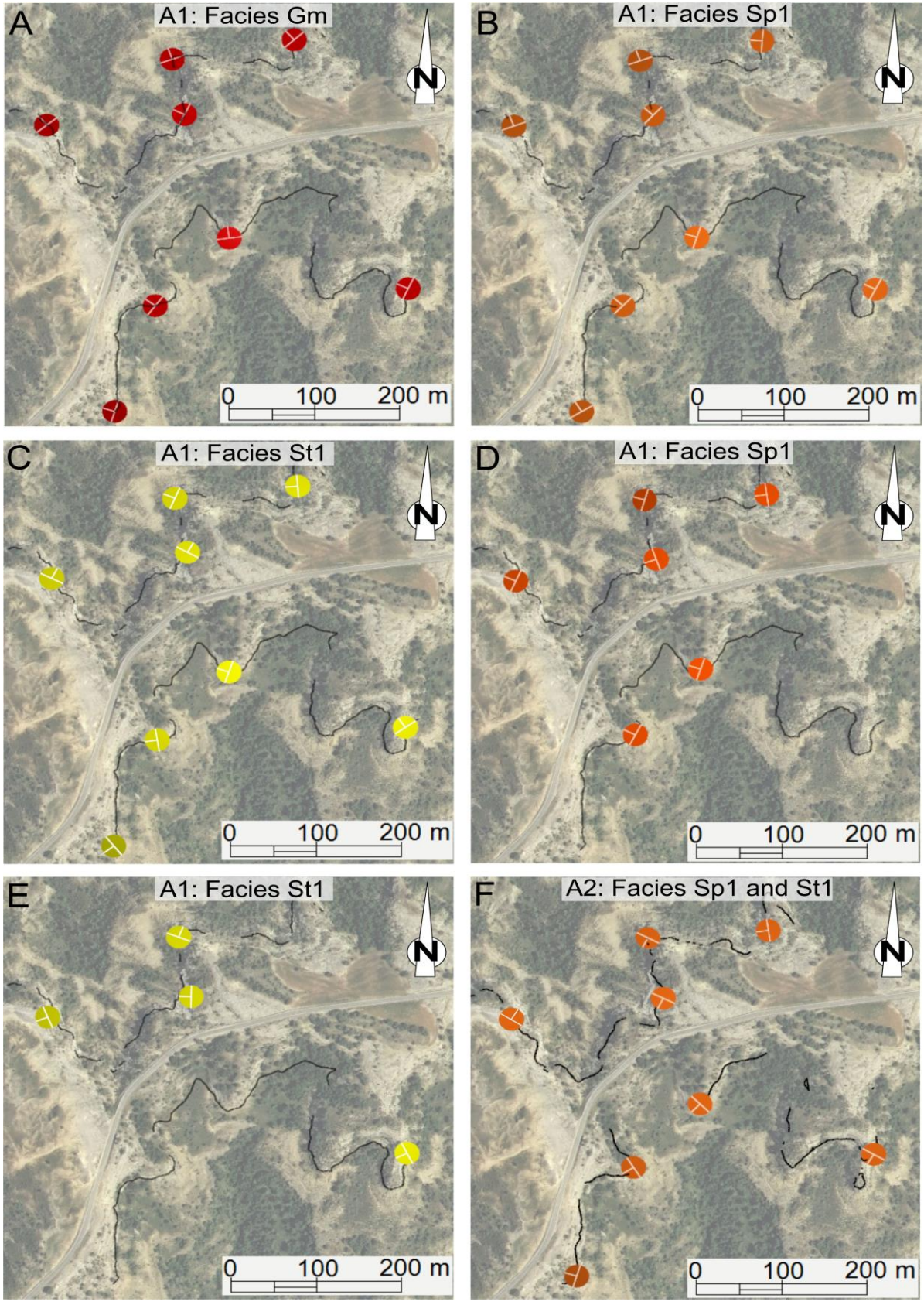
A
A1: Facies Gm
N
0 100 200 m
B
A1: Facies Sp1
N
0 100 200 m
C
A1: Facies St1
N
0 100 200 m
D
A1: Facies Sp1
N
0 100 200 m
E
A1: Facies St1
N
0 100 200 m
F
A2: Facies Sp1 and St1
N
0 100 200 m

Figure 7B

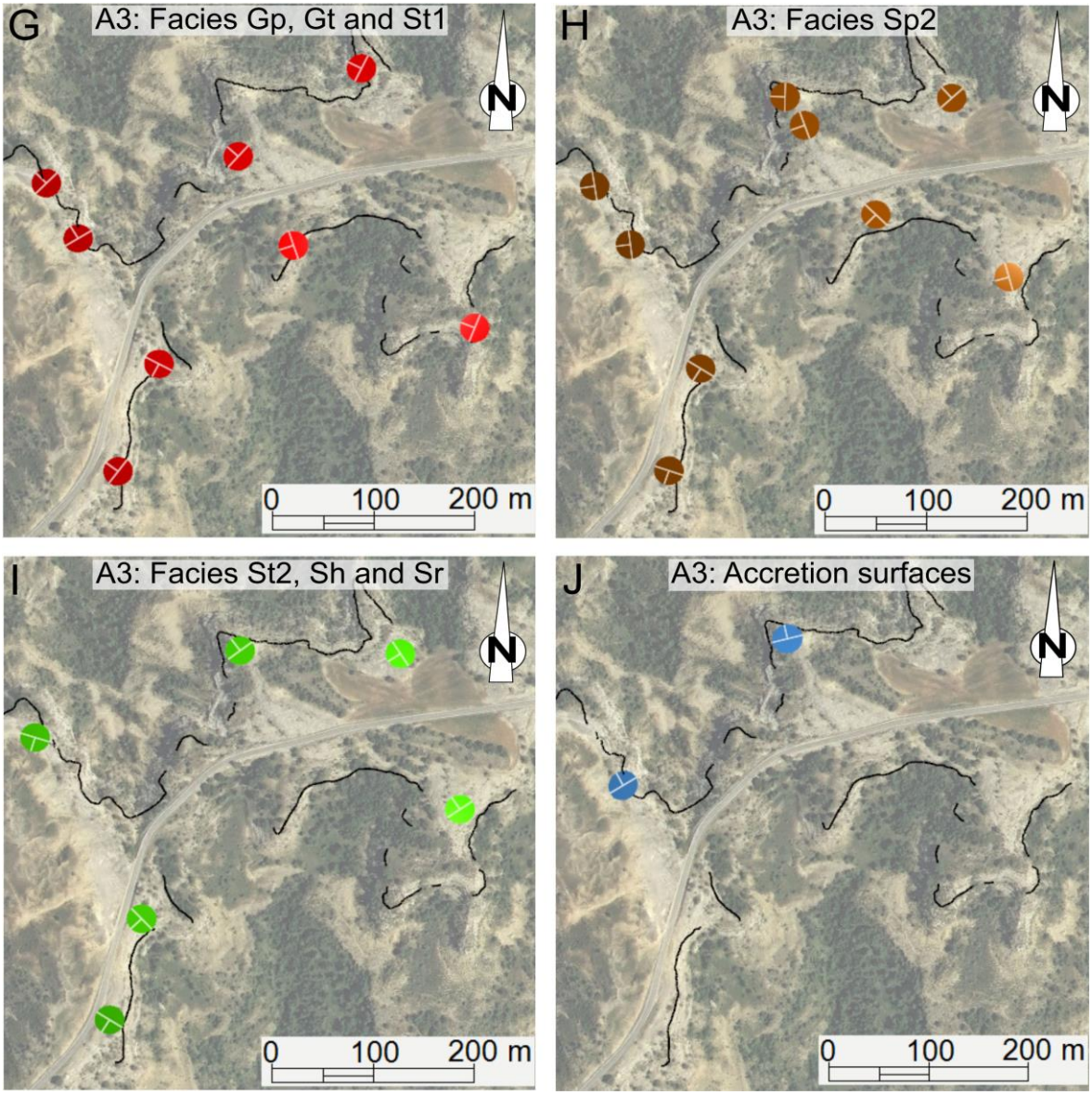
G
A3: Facies Gp, Gt and St1
N
0 100 200 m
H
A3: Facies Sp2
N
0 100 200 m
I
A3: Facies St2, Sh and Sr
N
0 100 200 m
J
A3: Accretion surfaces
N
0 100 200 m

Figure 8

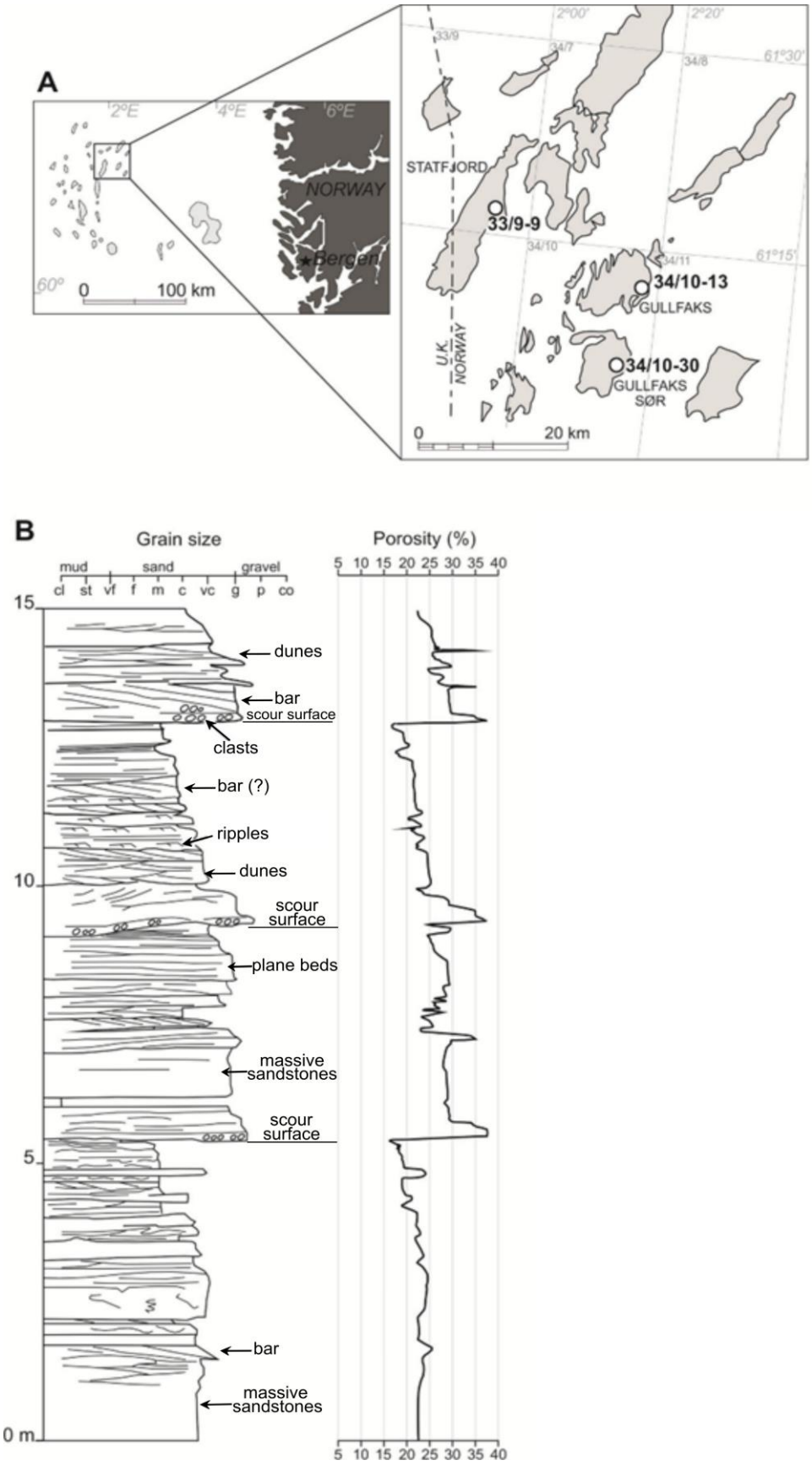
A
2°E
4°E
6°E
NORWAY
Bergen
60°
0
100 km
2°00'
2°20'
33/9
34/7
34/8
61°30'
STATFJORD
33/9-9
34/10
34/11
61°15'
34/10-13
GULLFAKS
U.K.
NORWAY
34/10-30
GULLFAKS
SØR
0
20 km
B
Grain size
mud
sand
gravel
cl st vf f m c vc g p co
Porosity (%)
5 10 15 20 25 30 35 40
15
10
5
0 m
dunes
bar
scour surface
clasts
bar (?)
ripples
dunes
scour surface
plane beds
massive sandstones
scour surface
bar
massive sandstones

Figure 9

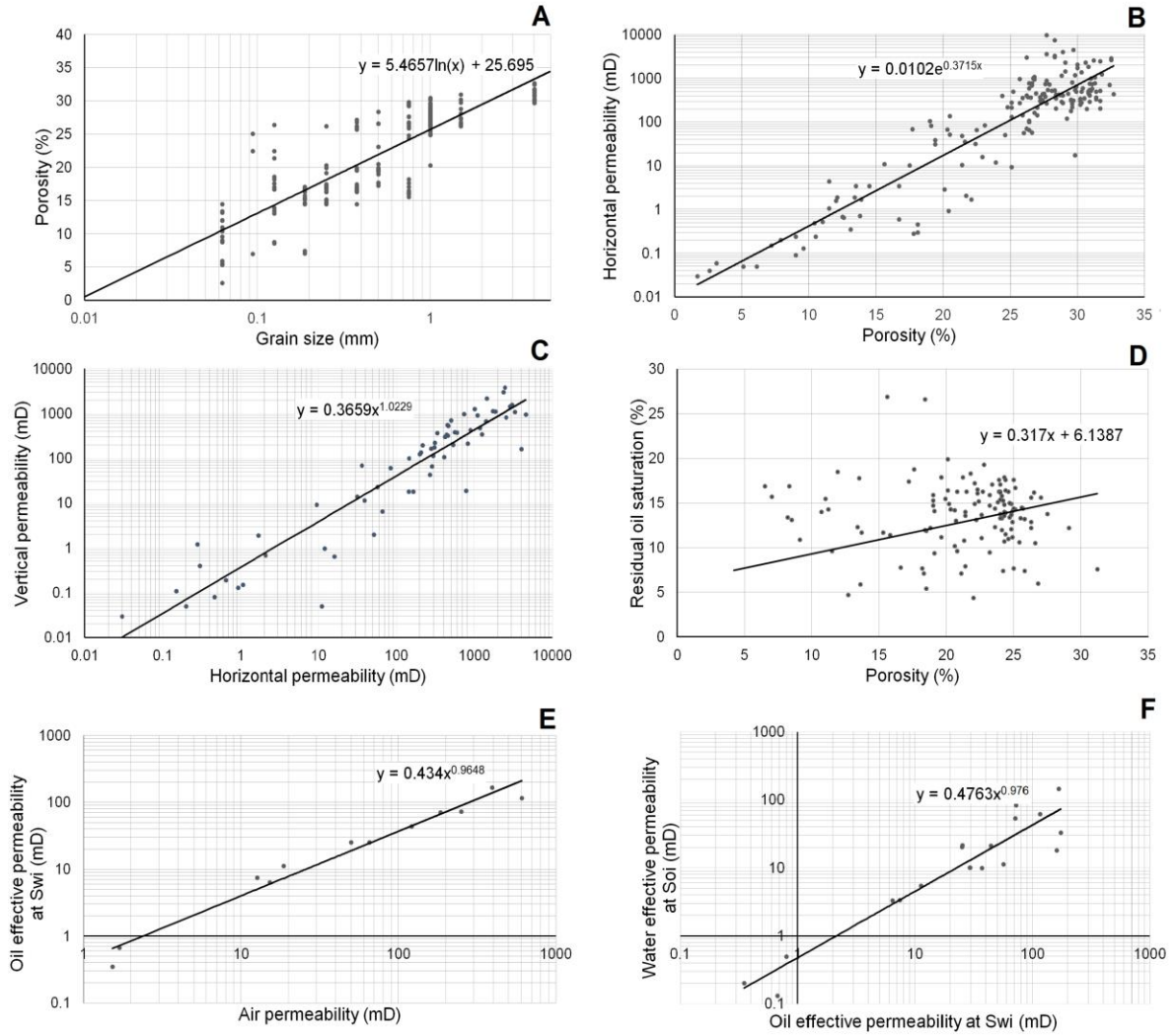
A
y = 5.4657ln(x) + 25.695
Porosity (%)
Grain size (mm)
B
y = 0.0102e^0.3715x
Horizontal permeability (mD)
Porosity (%)
C
y = 0.3659x^1.0229
Vertical permeability (mD)
Horizontal permeability (mD)
D
y = 0.317x + 6.1387
Residual oil saturation (%)
Porosity (%)
E
y = 0.434x^0.9648
Oil effective permeability at Swi (mD)
Air permeability (mD)
F
y = 0.4763x^0.976
Water effective permeability at Soi (mD)
Oil effective permeability at Swi (mD)

Figure 10

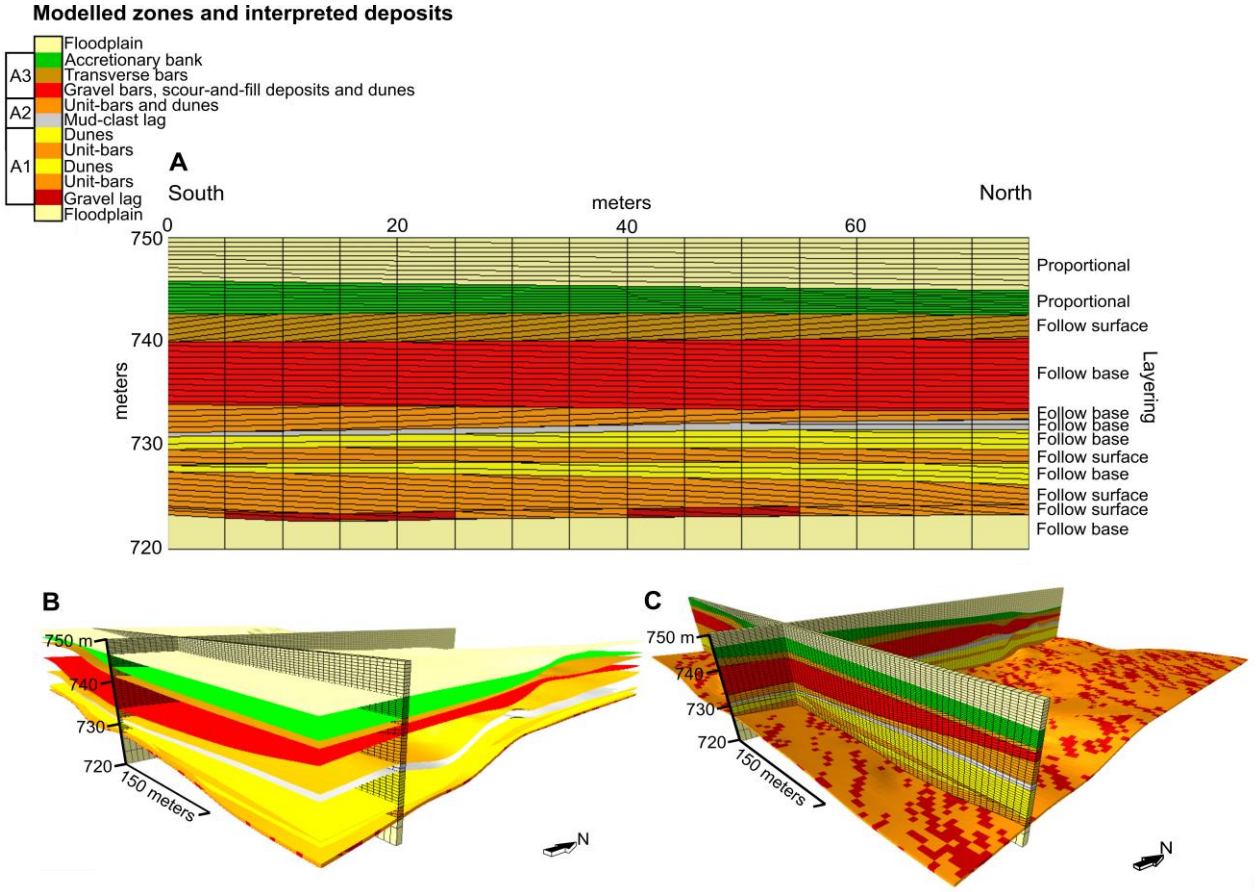
Modelled zones and interpreted deposits
Floodplain
Accretionary bank
Transverse bars
Gravel bars, scour-and-fill deposits and dunes
Unit-bars and dunes
Mud-clast lag
Dunes
Unit-bars
Dunes
Unit-bars
Gravel lag
Floodplain
A3
A2
A1
A
South
North
meters
0
20
40
60
750
740
730
720
meters
Proportional
Proportional
Follow surface
Follow base
Follow base
Follow base
Follow base
Follow surface
Follow base
Follow surface
Follow surface
Follow base
Layering
B
750 m
740
730
720
150 meters
N
C
750 m
740
730
720
150 meters
N

Figure 11

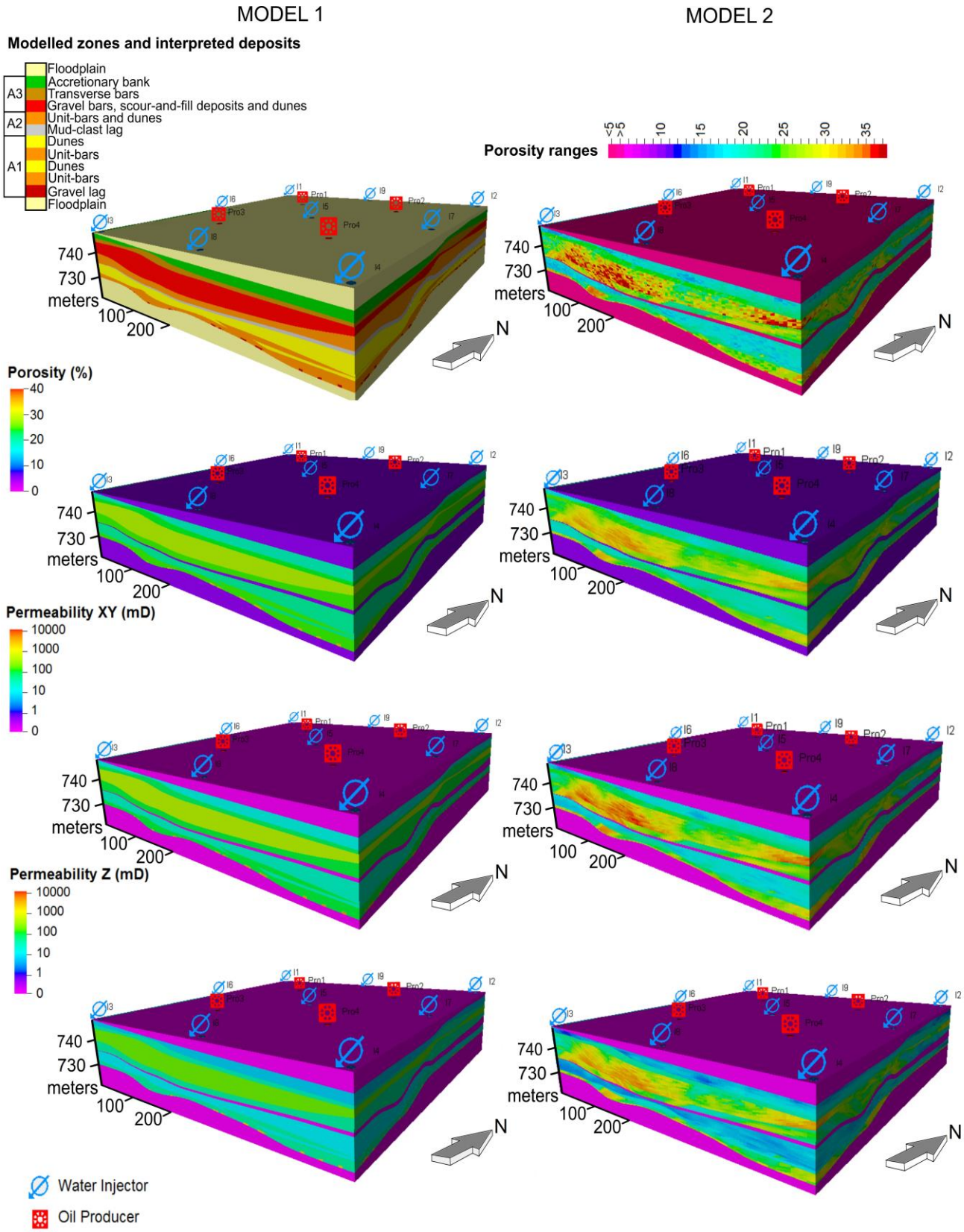
MODEL 1
MODEL 2
Modelled zones and interpreted deposits
A3
A2
A1
Floodplain
Accretionary bank
Transverse bars
Gravel bars, scour-and-fill deposits and dunes
Unit-bars and dunes
Mud-clast lag
Dunes
Unit-bars
Dunes
Unit-bars
Gravel lag
Floodplain
Porosity ranges
<5
>5
10
15
20
25
30
35
740
730
meters
100
200
N
Porosity (%)
40
30
20
10
0
Permeability XY (mD)
10000
1000
100
10
1
0
Permeability Z (mD)
10000
1000
100
10
1
0
Water Injector
Oil Producer

Figure 12

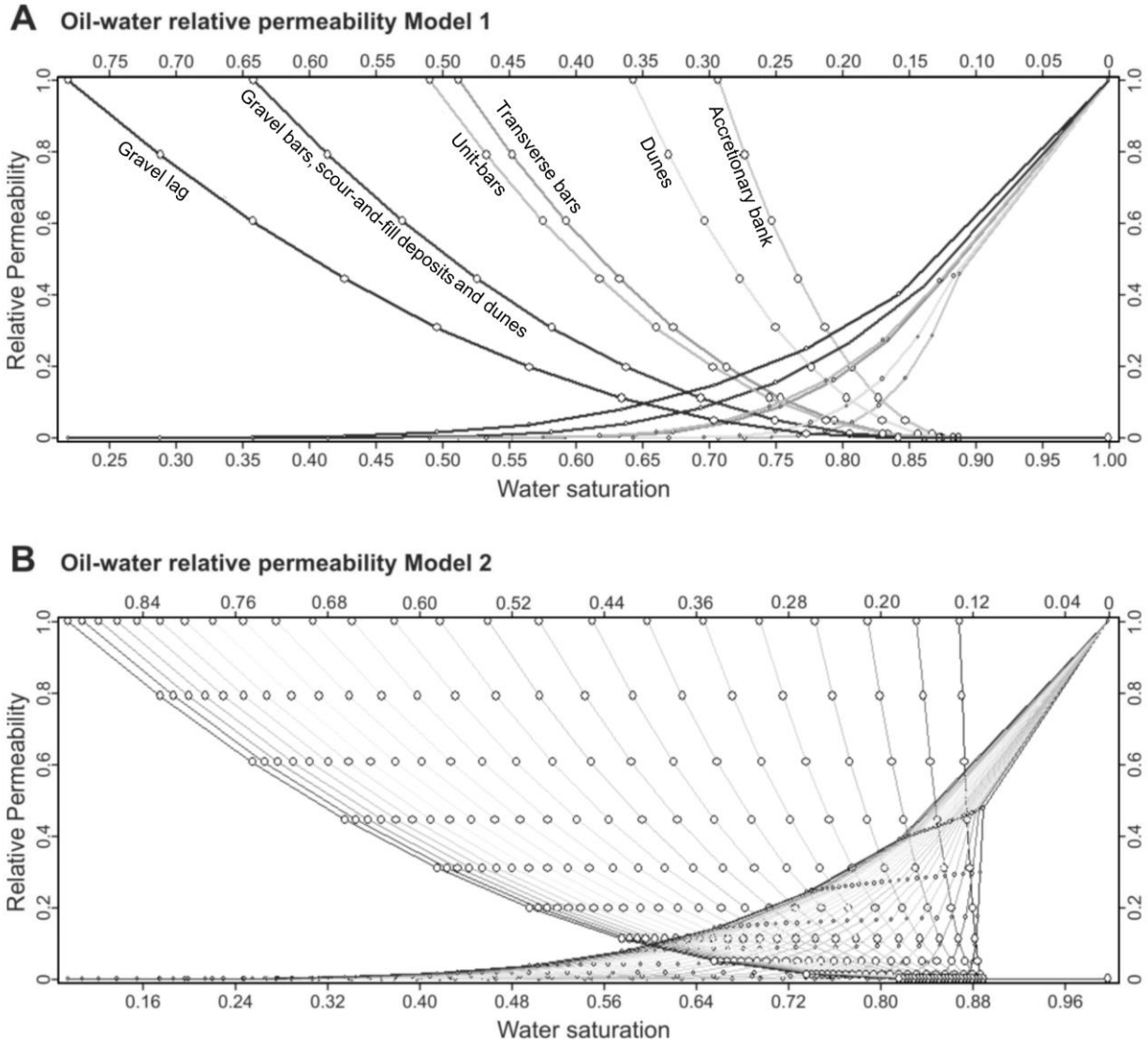
A
Oil-water relative permeability Model 1
Relative Permeability
Water saturation
Gravel lag
Gravel bars, scour-and-fill deposits and dunes
Unit-bars
Transverse bars
Dunes
Accretionary bank
B
Oil-water relative permeability Model 2
Relative Permeability
Water saturation

Figure 13

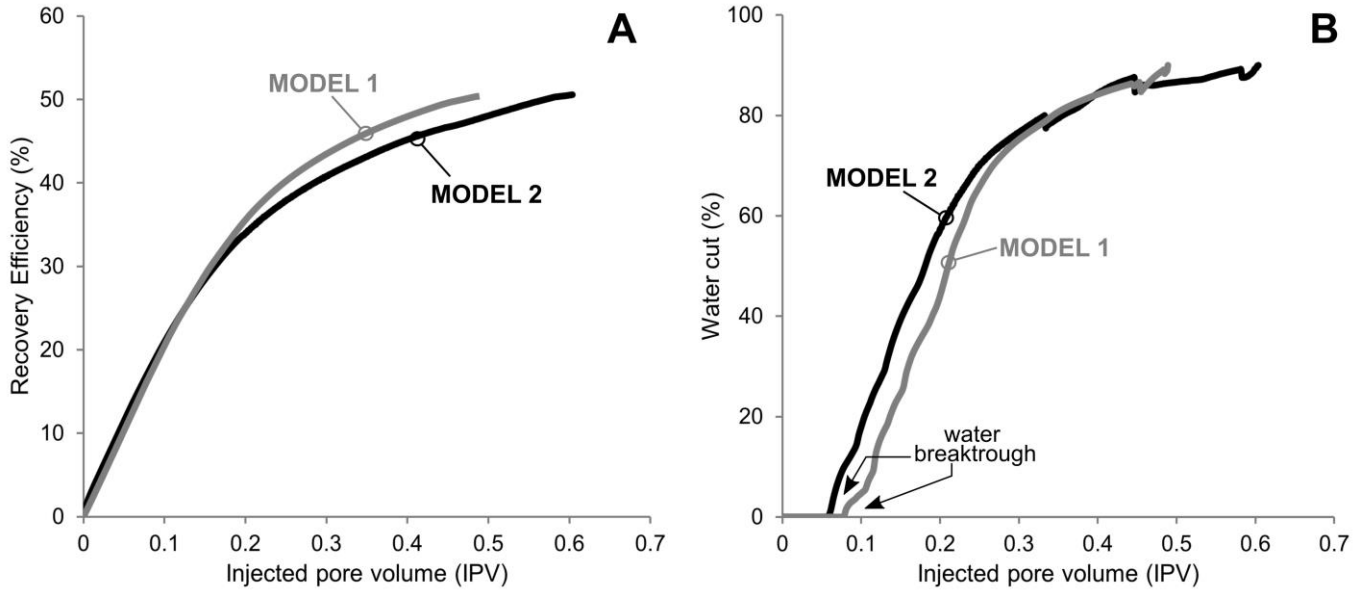
A
MODEL 1
MODEL 2
Recovery Efficiency (%)
Injected pore volume (IPV)
B
MODEL 2
MODEL 1
water
breaktrough
Water cut (%)
Injected pore volume (IPV)

Figure 14

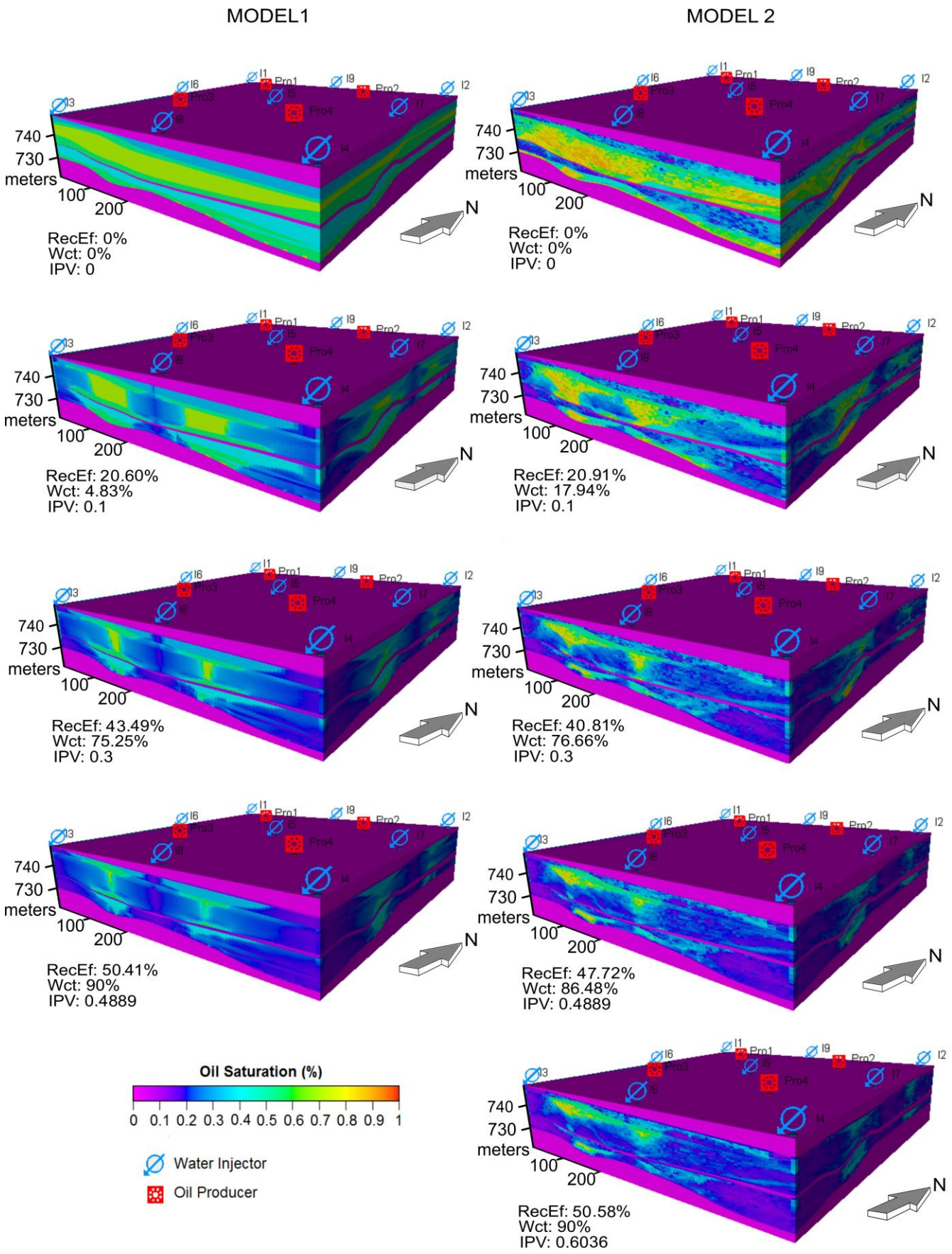
MODEL1
MODEL 2
740
730
meters
100
200
N
RecEf: 0%
Wct: 0%
IPV: 0
RecEf: 0%
Wct: 0%
IPV: 0
RecEf: 20.60%
Wct: 4.83%
IPV: 0.1
RecEf: 20.91%
Wct: 17.94%
IPV: 0.1
RecEf: 43.49%
Wct: 75.25%
IPV: 0.3
RecEf: 40.81%
Wct: 76.66%
IPV: 0.3
RecEf: 50.41%
Wct: 90%
IPV: 0.4889
RecEf: 47.72%
Wct: 86.48%
IPV: 0.4889
Oil Saturation (%)
0 0.1 0.2 0.3 0.4 0.5 0.6 0.7 0.8 0.9 1
Water Injector
Oil Producer
RecEf: 50.58%
Wct: 90%
IPV: 0.6036

Figure 15

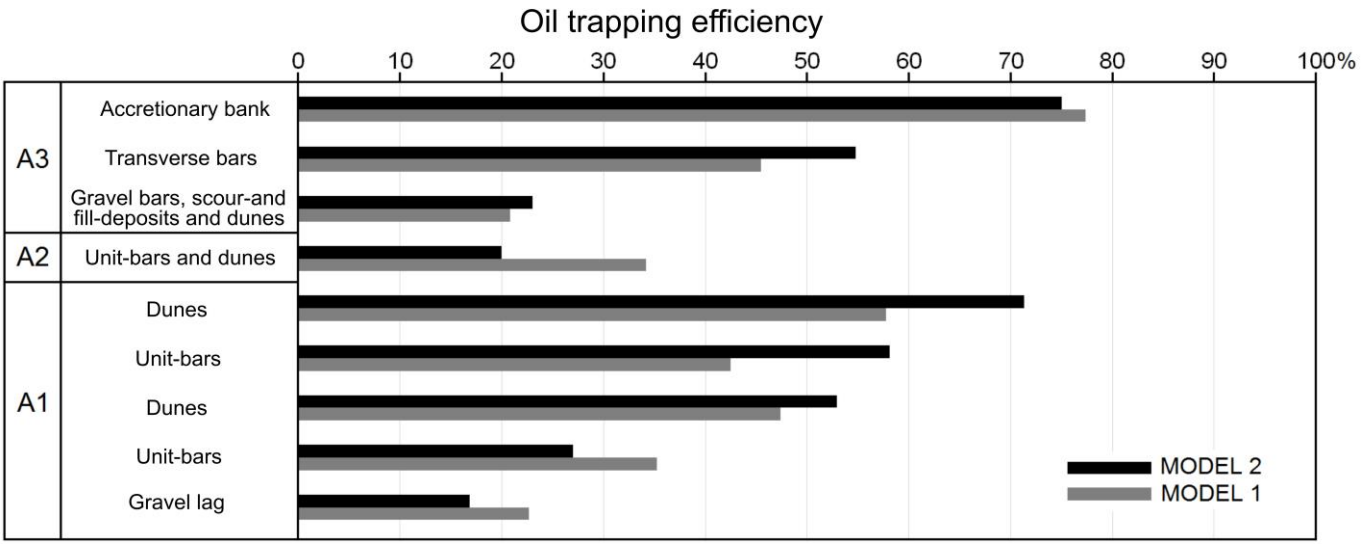

Table 1

Facies	***Description***	***Interpreted mesoform***
Mcgl	Massive, structureless, located at the base of 1 to 2 m depth scoured surfaces. Mud-clast conglomerate, clasts are black coloured, from 1 to 10 cm. Clasts roundness ranges from sub-angular to sub-rounded. The deposit is 0.2 to 1.5 m thick. Blocks of mud up to 50 cm large may be present. Subordinate amounts of pebbles.	Mud-clast channel lag (Rip-up clasts from old floodplain deposits) (Garzanti, 1991; Henares *et al.,* 2016)
Gm	Massive or crudely bedded gravels, located at the base of scoured surface. Clast-supported pebble-to-cobble conglomerate. Clasts are rounded to sub-rounded. The deposit is 0.6 to 2.6 m thick. Subordinate mud-clasts, oxidized wood fragments and minor amounts of sand within the matrix.	Gravel channel lag (Miall, 1977, 1978, 1988; Viseras *et al.,* 2009)
Gt/Gp	Large and small scale, low angle, trough and planar cross-stratified gravels. Pebbly dominated, locally cobble size. Clasts are rounded to sub-rounded. Beds from 0.5 to 1.5 m thick, bed-sets from 1 to 3 m thick. Minor amounts of interbedded pebbly to upper medium sandstones.	Gravel bars and scour and fill deposits (Miall, 1977, 1978, 1988; Nijman and Puigdefàbregas, 1978; Viseras *et al.,* 2006)
Sp1	Large scale planar cross-stratified sandstones. Pebbly-to-coarse sandstone. Groups of 1 to 4 beds; beds from 0.4 to 3 m thick, bed-sets from 0.5 to 3.5 m thick. Beds commonly show a fining upward trend. Subordinate mud-clasts or oxidized wood fragments up to 1 m large have been observed.	Bars (linguoid or transverse) (Collinson, 1970; Miall, 1977, 1978, 1988; Viseras *et al.,* 2009) Unit-bars (Reesink and Bridge 2007, 2011)
Sp2	Large scale planar cross-stratified sandstones. From upper coarse to upper medium sandstone. Multiple beds, 1 to 3. Beds thickness from 0.4 to 1.5 m, bed-sets from 1 to 3 m thick. Beds commonly show a fining upward trend. No secondary components.	Transverse bars (Nijman and Puigdefàbregas, 1978) Unit-bars (Reesink and Bridge 2007, 2011)
St1	Small scale trough cross-stratified sandstones. Pebbly-to-medium sandstone. Beds are 20 to 60 cm thick, forming bed-sets from 0.3 to 2.5 m thick. Subordinate amounts of pebbles and laminaes of oxidized OM.	Dunes (Collinson, 1970; Miall, 1977, 1978, 1988; Viseras *et al.,* 2009)
St2	Small scale trough cross-stratified sandstones. Coarse-to-medium sandstones. Beds are 20-30 cm thick, forming bed-sets from 0.4 to 1.5 m thick. Intense mottling.	Dunes (Festoons) (Nijman and Puigdefàbregas, 1978)
Sr	Asymmetrical current ripples. Fine sandstones. Facies is 10 to 30 cm thick. Intense mottling.	Rippled sands (Collinson, 1970; Miall, 1977, 1978, 1988)
Sh	Low angle-irregularly planar-laminated sandstone. Medium-to-fine dominated sandstone. Facies is 0.5 to 1 m thick. Intense mottling.	Planar beds (lower flow regime) (Miall, 1978, 1978)
Fm	Massive or interbedded. Muddy-silty dominated. The deposit is up to 6 m thick. Intense mottling.	Floodplain deposits (Miall, 1977, 1978, 1988)

Table 2

Story	*Facies*	*Interpreted form*
Downstream accreting/ Channel fill	Gm-Sp-St	Compound bar or channel fill (Ashworth *et al.*, 2011; Ford and Pyles, 2014)
Laterally accreting	Gt, Gp, St1,Sp2, St2, Sr, Sh	Point bar (Ford and Pyles, 2014)

Table 3

Channel belt	*Modelled zones*	*Facies*					*Model 1 (Constant values)*			*Model 2 (SGS)*			
							Porosity (%)	*Permeability (mD)*		*Variogram function*	*Variogram range (m)*		
								Horizontal	*Vertical*		*Major direction*	*Minor direction*	*Vertical*
	Upper floodplain	Fm					5	0.01	0.01	-	Constant values of Model 1		
A3	Accretionary bank	St2,Sh,Sr					19.34	13.48	5.25	Spherical	405	85	7.1
	Transverse bars	Sp2					23.85	72.05	29.07	Spherical	117	112	1.64
	Gravel bars, scour-and-fill deposits and dunes	Gt,Gp, St1					28.29	374.97	157.14	Gaussian	220	99	19.6
A2	Unit-bars and dunes	Sp1,St1					24.38	88.11	35.72	Spherical	292	128	3.64
	Mud-clast lag	Mcgl					5	0.01	0.01	-	Constant values of Model 1		
A1	Dunes	St1					20.77	22.92	9.01	Spherical	263	73	5.17
	Unit-bars	Sp1					24.38	88.11	35.72	Spherical	164	62	1.19
	Dunes	St1					20.77	22.92	9.01	Gaussian	272	205	7.9
	Unit-bars	Sp1					24.38	88.11	35.72	Spherical	324	310	5.5
	Gravel lag	Sp1	Proportion	70%			24.38	88.11	35.72		Constant values of Model 1		
		Gm	Proportion	30%			35	4019	1778	Spherical	152	136	0.62
			Object-based	Lower half pipe shape									
			Dimensions	Min	Mean	Max							
			Minor width (m)	0.3	0.5	1							
			Major/Minor ratio	3	5	10							
			Thickness (m)	0.6	0.9	2.6							
	Lower floodplain	Fm					5	0.01	0.01	-	Constant values of Model 1		